JGR Oceans

RESEARCH ARTICLE
10.1029/2023JC020859

Interactions of Remotely Generated Internal Tides With the U.S. West Coast Continental Margin

Oladeji Q. Siyanbola[1], Maarten C. Buijsman[1], Audrey Delpech[2], Roy Barkan[2,3], Yulin Pan[4], and Brian K. Arbic[5]

[1]School of Ocean Science and Engineering, University of Southern Mississippi, Stennis Space Center, MS, USA, [2]Department of Atmospheric and Ocean Science, UCLA, Los Angeles, CA, USA, [3]Porter School of the Environment and Earth Sciences, Tel Aviv University, Ramat Aviv, Israel, [4]Department of Naval Architecture and Marine Engineering, University of Michigan, Ann Arbor, MI, USA, [5]Department of Earth and Environmental Sciences, University of Michigan, Ann Arbor, MI, USA

Abstract Through interactions with the continental margins, incident low-mode internal tides (ITs) can be reflected, scattered to high modes, transmitted onto the shelf and dissipated. We investigate the fate of remotely generated mode-1 ITs in the U.S. West Coast (USWC) continental margin using two 4-km horizontal resolution regional simulations. These 1-year long simulations have realistic stratification, and atmospheric, tidal, and subtidal forcings. In addition, one of these simulations has remote internal wave (IW) forcing at the open boundaries while the other does not. To compute the IT reflectivity of the USWC margin, we separate the IT energy fluxes into onshore and offshore propagating components using a Discrete Fourier Transform in space and time. Overall, ∼20% of the remote mode-1 semidiurnal IT energy fluxes reflect off the USWC margin, 40% is scattered to modes 2–5, and 7% is transmitted onto the shelf while the remaining is dissipated on the continental slope. Furthermore, our results reveal that differences in stratification, slope criticality, topographic roughness and angle of incidence cause these fractions to vary spatially and temporally along the USWC margin. However, there is no clear seasonal variability in these estimates. Remote IWs enhance the advection and diffusion of heat in the continental margin, resulting in cooling at the surface and warming at depth, and a reduction in the thermocline stratification. These results suggest that low-mode ITs can cause water mass transformation in continental margins that are far away from their generation sites.

Plain Language Summary Ocean dynamics that exist over a wide range of spatial scales, such as the internal tides (ITs), are best resolved in numerical simulations with fine grid spacings. To accomplish this, model solutions are downscaled by nesting domains with increasingly higher resolution. However, the long propagation distances of low-mode ITs away from their generation sites necessitate their inclusion at the open boundaries of regional simulations. Here, we show that these remotely generated ITs, for example, from Hawaii, modulate turbulence in the U.S. West Coast (USWC) continental margin. Approximately 80% of the remote mode-1 semidiurnal IT energy is available for mixing in the USWC margin. In the absence of an accurate IT forcing at the open boundaries of coastal regional models, IT mixing may be underestimated.

Key Points:

- The bulk of the internal tide (IT) energy approaching the U.S. West Coast comes from far-field sources, for example, Hawaii
- On average, 20% of the remote mode-1 IT energy is reflected while the remaining energy is scattered to higher modes and dissipated
- The remote ITs advect and diffuse heat in the continental margin, causing surface cooling and subsurface warming

Correspondence to:
O. Q. Siyanbola,
oladeji.siyanbola@usm.edu

Citation:
Siyanbola, O. Q., Buijsman, M. C., Delpech, A., Barkan, R., Pan, Y., & Arbic, B. K. (2024). Interactions of remotely generated internal tides with the U.S. West Coast continental margin. *Journal of Geophysical Research: Oceans*, *129*, e2023JC020859. https://doi.org/10.1029/2023JC020859

Received 23 DEC 2023
Accepted 29 MAY 2024
Corrected 5 JUL 2024

This article was corrected on 5 JUL 2024. See the end of the full text for details.

Author Contributions:
Conceptualization: Oladeji Q. Siyanbola, Maarten C. Buijsman
Formal analysis: Oladeji Q. Siyanbola, Maarten C. Buijsman
Funding acquisition: Maarten C. Buijsman, Roy Barkan, Brian K. Arbic
Investigation: Oladeji Q. Siyanbola, Maarten C. Buijsman
Methodology: Oladeji Q. Siyanbola, Maarten C. Buijsman
Project administration: Maarten C. Buijsman
Resources: Roy Barkan
Software: Audrey Delpech, Roy Barkan
Supervision: Maarten C. Buijsman

1. Introduction

Although continental margins (i.e., the ocean-continent boundaries) occupy a modest proportion of the global ocean (28% by area; Symonds et al., 2000), they are highly relevant for numerous physical and bio-geo-chemical processes (e.g., Babu et al., 2002; Muller-Karger et al., 2005; Townsend et al., 2004; Whitney et al., 2005). Water masses, sediments and nutrients in the continental margins are modulated by river discharges (e.g., Bianchi et al., 2010; Cohen et al., 2014; Hill et al., 2007; Lehrter et al., 2013; Mouyen et al., 2018), and by several oceanic processes such as mesoscale eddies (e.g., Chen et al., 2019; Yang et al., 2019; Zhang et al., 2022), submesoscale currents (e.g., Barkan et al., 2017; T. Wang et al., 2021), tidal and subtidal currents (e.g., Hermann et al., 2002; Spicer et al., 2021), hydraulic flows (e.g., Dorrell et al., 2016; Holland et al., 2002), and by internal waves (IWs, e.g., Friedrichs & Wrights, 1995; Miramontes et al., 2020; Villamaña et al., 2017).

IWs in the ocean are generated by the interaction of tidal currents with the topography (internal tides—ITs, e.g., Buijsman et al., 2020; Falahat et al., 2014; Niwa & Hibiya, 2014; Zhao et al., 2016; Zhang et al., 2017), wind forcing (near inertial waves—NIWs, e.g., Alford et al., 2016; Cyriac et al., 2022; Raja et al., 2022; Shen et al., 2020), and mesoscale turbulence (e.g., Clément et al., 2016; Han, 2022; Johannessen et al., 2019;

Visualization: Oladeji Q. Siyanbola, Maarten C. Buijsman
Writing – original draft: Oladeji Q. Siyanbola, Maarten C. Buijsman
Writing – review & editing: Oladeji Q. Siyanbola, Maarten C. Buijsman, Audrey Delpech, Roy Barkan, Yulin Pan, Brian K. Arbic

Voisin, 1992). While high-mode IWs are most susceptible to breaking at their generation sites (Klymak et al., 2008), low-mode IWs tend to propagate across the ocean basins before they eventually dissipate (e.g., Kerry et al., 2013; Simmons & Alford, 2012; Siyanbola et al., 2023; Waterhouse et al., 2014; Zaron, 2019).

In an effort to map the geography of IW dissipation in the global ocean, Waterhouse et al. (2014) used a compilation of microstructure profiles, density overturns and shear-strain measurements. They inferred that the majority (69%) of the IW energy dissipates in the deep ocean. Although the fractions differ, several global ocean circulation studies also find that the majority of IW energy is dissipated in the deep ocean. Eden and Olbers (2014) argued that more than 90% of the low-mode IT energy dissipation occurs in the open ocean due to parametric subharmonic instability and topographic scattering. Adopting the same framework as Eden and Olbers (2014), but using different wave-wave interaction and topographic scattering parameterizations, de Lavergne et al. (2019) estimated that ∼65%–80% of the low-mode IT energy dissipation takes place in the deep waters. Buijsman et al. (2016) found only 12% of the low-mode semidiurnal IT energy generated in the open ocean reaches the continental margins. In contrast, Kelly et al. (2013) suggested that the majority of the mode-1 semidiurnal IT energy dissipates at large topographic features, for example, the continental margins.

To understand how incident IWs interact with the continental margins, a number of idealized two-dimensional numerical experiments have been conducted in the past (e.g., Dauxois & Young, 1999; Legg, 2014; Legg & Adcroft, 2003; S. Wang et al., 2018). These studies have looked at factors that affect the fate of incident IWs, such as the shape of the continental slope, the presence of abrupt topographies, the slope criticality, and/or stratification. However, the aforementioned factors are known to vary spatially (both along- and cross-shore directions) and temporally in the real ocean. Prompted by an observation of a middepth pycnocline on the West Shetland slope, Hall et al. (2013) assessed the impacts of a cross-shore varying criticality on the reflectivity and transmissivity of incident IWs using a two-dimensional numerical model. The fate of incident IWs at the continental margins have also been studied using realistic three-dimensional numerical simulations but at regional scales (e.g., Gong et al., 2022; Kelly et al., 2012; Klymak et al., 2016; Masunaga et al., 2023; Osborne et al., 2011; S. Wang et al., 2021). Kelly et al. (2013) created a global map of mode-1 semidiurnal IT reflectivity, transmissivity and topographic scattering in the continental margins using a two-dimensional model that incorporates realistic topography and stratification. They estimated that the continental margins reflect 40% of the incident energy and scatter 40% to higher modes, while the remaining 20% is transmitted onto the continental shelves.

The breaking of incident IWs in the continental margins has been observed to cause increased turbulent diffusivities (e.g., Martini et al., 2013; Moum et al., 2002; Nash et al., 2007). While the turbulent diffusion is stronger near the topography where the incident IWs break, the vertical mixing can extend several hundreds of meters in the water column (Nash et al., 2007). As a result, tracers such as temperature and nutrients are redistributed. However, IW-induced advection (both vertical and horizontal) can also cause water mass transformation in the ocean. This has been demonstrated in the numerical studies of Jensen et al. (2020) and Assene et al. (2024), who both estimated that through vertical mixing and advection, heat can be redistributed along IWs propagation pathways. Also, from their mooring observations over the northern South China Sea continental slope, Liang et al. (2019) found both diffusion and advection to contribute to the temporal variability in vertical temperature profiles after the passage of internal solitary wave trains.

In this study, we investigate the fate of remote semidiurnal ITs in the U.S. West Coast (USWC) continental margin using realistically forced regional simulations. In addition, we evaluate the influence of the remote ITs on stratification and turbulent diffusivities. Unlike the studies of Kelly et al. (2012) and Suanda et al. (2017), which feature remote ITs from the Mendocino Escarpment and nearby rough topographies in the Santa Maria Basin, respectively, we also consider remote ITs radiating from sources thousands of kilometers away, for example, from Hawaii (Arbic et al., 2004; Buijsman et al., 2020; Dushaw et al., 1995; Ray & Mitchum, 1996; Zaron et al., 2022). In regional model simulations with high-frequency baroclinic forcing at the open boundaries, Siyanbola et al. (2023) showed that remotely generated ITs from Hawaii reach the USWC. We use their 1-year long (01 October 2011 to 30 September 2012) regional model solutions to address the following research questions: (a) What fraction of the remote ITs is reflected back to the open ocean, scattered to higher modes, dissipated, and transmitted onto the continental shelf? (b) How strong is the seasonal variability in the estimates in (a)? (c) What are the impacts of the remote ITs on stratification and turbulent diffusivities in the USWC margin?

The remainder of this paper is structured as follows. Section 2 provides a description of the numerical model setup of the 1-year simulations, IT energy balance, directional decomposition of the IT energy flux field, and IT modal

decomposition. In Section 3, we present results on directionally filtered semidiurnal IT energy fluxes, mode-1 IT reflectivity, scattering to modes 2–5, and transmission onto the shelf in the USWC margin, and how they vary seasonally. In Section 4, we provide a discussion on the spatial variability of our findings and the impact of the remote ITs on heat redistribution, stratification, and turbulent diffusivities. Our conclusions are presented in Section 5.

2. Methods

2.1. ROMS Model

In this study, we use the Regional Ocean Modeling System (ROMS; Shchepetkin & McWilliams, 2005, 2009) simulation of the ocean near the U.S. West Coast (USWC; Siyanbola et al., 2023). This simulation has a 4-km horizontal grid resolution with 60 σ-layers. The simulation uses the surface and bottom stretching parameters, $\theta_s = 6$ and $\theta_b = 3$, and pycnocline depth, $h_c = 250$ m. At the lateral open boundaries, the regional simulation is forced with surface tides and remotely generated IWs from a global HYbrid Coordinate Ocean Model (HYCOM; Bleck et al., 2002) simulation that includes both tidal and atmospheric forcing (Arbic et al., 2010, 2012, 2018; Buijsman et al., 2017, 2020). It also receives subtidal forcing from a basin scale ROMS simulation of the Northeast Pacific (Renault et al., 2021). To minimize IW reflections at the open boundaries from the interior, the simulation uses a 58-km wide sponge layer with a maximum horizontal viscosity of 800 m^2/s. This simulation is run from 1 October 2011 to 30 September 2012. Henceforth, we will refer to this simulation as WRIT (With Remote ITs), and the ITs radiating into the domain through the open boundaries as "Remote ITs." For comparison purposes, we also use a twin simulation but without remote IW forcing referred to as NRIT (No Remote ITs). Furthermore, both the WRIT and NRIT solutions have realistic atmospheric, river runoff climatology and tidal forcing. For further details on these simulations, refer to Siyanbola et al. (2023).

2.2. Undecomposed IT Energy Balance

Although Siyanbola et al. (2023) found NIWs to be equally important as the semidiurnal ITs at the open boundaries, little remote NIW energy flux reaches the USWC margin. Therefore in this study, our focus will be on the semidiurnal ITs. We extract the semidiurnal ITs by bandpassing the pressure perturbation (p') and the baroclinic horizontal velocity vector $\left(\mathbf{u}' = u'\hat{i} + v'\hat{j}\right)$ with a 9–15 hr Butterworth filter. $\hat{i}$ and $\hat{j}$ are the unit vectors along the x- and y-directions, respectively. Positive x is directed toward the shore and positive y is directed approximately along the shore toward northwest. The IT energy balance can be expressed as (Buijsman et al., 2012; Carter et al., 2008; Kerry et al., 2013)

$$C = \nabla \cdot \mathbf{F} + D_v + \mathcal{R}. \tag{1}$$

To contrast with the energy balance decomposed into vertical modes, we refer to this balance as the undecomposed IT energy balance. The barotropic-to-baroclinic energy conversion

$$C = \langle p'|_{z=-H} \mathbf{U} \cdot \nabla(-H) \rangle, \tag{2}$$

where H is the seafloor depth, $p'|_{z=-H}$ is the near-bottom pressure perturbation, $\mathbf{U}$ is the barotropic velocity, $\nabla = \frac{\partial}{\partial x}\hat{i} + \frac{\partial}{\partial y}\hat{j}$, and $\langle .. \rangle$ represents time averaging. Unless otherwise stated, time averaging in this paper is done on monthly basis. The second term $\nabla \cdot \mathbf{F}$ is the energy flux divergence, and the depth-integrated IT energy flux

$$\mathbf{F} = \int_{-H}^{0} \langle p'\mathbf{u}' \mathrm{d}z \rangle. \tag{3}$$

The energy dissipation term due to vertical eddy viscosity (Buijsman et al., 2012)

$$D_v = \rho_0 \int_{-H}^{0} \langle \epsilon \ \mathrm{d}z \rangle = \rho_0 \int_{-H}^{0} \left\langle A_v \left(\left(\frac{\partial u'}{\partial z} \right)^2 + \left(\frac{\partial v'}{\partial z} \right)^2 \right) \mathrm{d}z \right\rangle, \tag{4}$$

where $\rho_0 = 1027.4\ \mathrm{kg/m^3}$, ϵ is the turbulent dissipation rate and A_v is the vertical eddy viscosity. We do not include horizontal viscosity contributions in Equation 4 because ROMS does not have an explicit horizontal eddy viscosity (Haidvogel et al., 2000; Shchepetkin & McWilliams, 2003). This implies that the actual dissipation of ITs is more than that inferred from Equation 4. However, the implicit horizontal dissipation is much weaker than the vertical dissipation near USWC (Delpech et al., 2024). In addition, we note that the modeled dissipation may be sensitive to the model resolution and dissipation parameters (Kang & Fringer, 2012; Masunaga et al., 2018). The last term $\mathcal{R}$ in Equation 1 includes the energy tendency term, implicit horizontal dissipation, wave-mean flow and wave-wave interaction terms, and other offline computation errors.

Although vertical mixing in the NRIT and WRIT simulations is parameterized using the K-Profile Parameterization scheme (KPP; Large et al., 1994), only the vertical eddy viscosity (A_v) was stored. We compute the vertical mixing diffusivity coefficient indirectly from ϵ as (Osborn, 1980)

$$\kappa = \frac{\Gamma \epsilon}{N^2}, \tag{5}$$

where the mixing efficiency $\Gamma = 0.2$ and N is the buoyancy frequency. However, in the mixed layer and near the seabed, we obtain unrealistically high diffusivity estimates when Γ is set to a constant value of 0.2. In the boundary layers, we calculate the mixing efficiency as (Wakata, 2018)

$$\Gamma = \frac{\chi Ri_g}{1 - \chi Ri_g}, \tag{6}$$

where Ri_g is the gradient Richardson number $\left(\frac{N^2}{\left(\frac{\partial u'}{\partial z}\right)^2 + \left(\frac{\partial v'}{\partial z}\right)^2}\right)$ and $\chi = 1.79$.

2.3. IT Energy Flux Directional Decomposition

To quantify the IT energy flux reaching and leaving the USWC margin, we directionally decompose the complex IT signals near the USWC with a Discrete Fourier Transform (DFT) technique (Gong et al., 2021, 2022; Mercier et al., 2008; Siyanbola et al., 2023). The depth-integrated IT energy flux can be expressed as

$$\mathbf{F} = \underbrace{\int_{-H}^{0} \langle p'_{\mathrm{on}} \mathbf{u}'_{\mathrm{on}} \mathrm{d}z \rangle}_{\mathbf{F}_{\mathrm{on}}} + \underbrace{\int_{-H}^{0} \langle p'_{\mathrm{off}} \mathbf{u}'_{\mathrm{off}} \mathrm{d}z \rangle}_{\mathbf{F}_{\mathrm{off}}} + \underbrace{\int_{-H}^{0} \langle p'_{\mathrm{off}} \mathbf{u}'_{\mathrm{on}} \mathrm{d}z \rangle + \int_{-H}^{0} \langle p'_{\mathrm{on}} \mathbf{u}'_{\mathrm{off}} \mathrm{d}z \rangle}_{\mathbf{F}_{\mathrm{x}}}, \tag{7}$$

where $\mathbf{F}_{\mathrm{on}}$, $\mathbf{F}_{\mathrm{off}}$, and $\mathbf{F}_{\mathrm{x}}$ are the time-mean onshore (eastward), offshore (westward) propagating, and the cross-term energy fluxes, respectively. We define the onshore components such that $-90 \leq \tan^{-1}\frac{l}{k} < 90$, where (k, l) is the wavenumber vector relative to the ROMS grid. The local x-axis is at an angle of 28.7° in an anticlockwise manner relative to the east. For the offshore components, $90 \leq \tan^{-1}\frac{l}{k} < 270$. A baroclinic sea surface height animation showing the undecomposed, onshore and offshore propagating mode-1 semidiurnal ITs near the USWC obtained using the DFT technique is shown in https://www.youtube.com/watch?v=XKcz7AnJn2s.

We estimate the IT reflectivity of the continental margin as

$$R = \frac{F_{\mathrm{r}}}{F_{\mathrm{in}}}, \tag{8}$$

where F_{in} and F_{r} are the time-mean and along-shore integrated incident and reflected IT energy fluxes perpendicular to the continental margin, respectively (see Section 3.3). While the DFT technique performs satisfactorily in decomposing complex IT fields into different directions, amplitude and/or phase errors will occur at the boundaries of the numerical domain (Klymak et al., 2016; Siyanbola et al., 2023). However, F_{in} and F_{r} in this study are obtained at the foot of the continental slope away from the boundaries. The foot of the continental slope coincides with the 2,500 and 3,000 m isobaths for the Washington and Oregon coast margins, respectively, and 3,500 m isobath for the Central and South California margins.

For an IT beam to be reflected back to the open ocean, the continental slope is required to be supercritical (Balmforth & Peacock, 2009). The slope criticality γ is defined as the ratio of the topography slope to the characteristic slope of an IT beam (Kelly et al., 2012; Kumar et al., 2019; Martini et al., 2011).

$$\gamma = |\nabla H|/s, \tag{9}$$

where the topography slope $|\nabla H| = \sqrt{(\partial H/\partial x)^2 + (\partial H/\partial y)^2}$, and the slope of the IT beam $s = \sqrt{\frac{\omega^2 - f^2}{N_b^2 - \omega^2}}$. N_b is the near-bottom buoyancy frequency, f is the local Coriolis frequency and ω is the tidal frequency. For a supercritical slope, $\gamma > 1$. An incident IT beam is forward-reflected and transmitted onshore if the slope is subcritical (i.e., $\gamma < 1$). A slope is critical to IT generation or scattering if $\gamma = 1$ (Bishakhdatta & Sutanu, 2011; Cacchione et al., 2002; Petrucino et al., 2002).

2.4. Projection of IT Motions Onto Vertical Modes

To better understand how the low-mode ITs reflect, scatter to higher modes, transmit onto the shelf, and dissipate in the USWC margin, we project the IT motions onto vertical modes (e.g., Gill & Clarke, 1974; Kelly, 2016; Kelly & Lermusiaux, 2016). The local vertical velocity/buoyancy eigenfunction Φ_n for mode n is obtained by solving the hydrostatic Stürm-Liouville problem (Gerkema & Zimmerman, 2008)

$$\frac{\partial^2 \Phi_n}{\partial z^2} + \frac{\langle N^2 \rangle}{c_n^2} \Phi_n = 0, \tag{10}$$

where c_n is the mode n eigenspeed. The horizontal baroclinic velocity/pressure perturbation eigenfunction

$$\phi_n = \frac{\partial \Phi_n}{\partial z}. \tag{11}$$

ϕ_n is normalized such that it satisfies the orthogonality condition (Kelly & Lermusiaux, 2016)

$$\int_{-H}^{0} \phi_m \phi_n \mathrm{d}z = H \delta_{mn}, \tag{12}$$

where δ_{mn} is the Kronecker delta. $\delta_{mn} = 1$ if $m = n$ and, 0 if $m \neq n$. The horizontal baroclinic velocity and pressure perturbation fields can be expressed as summations over infinite number of modes

$$\mathbf{u}'(\mathbf{x},z,t) = \sum_{n=1}^{\infty} \mathbf{u}'_n(\mathbf{x},t)\phi_n(\mathbf{x},z), \tag{13}$$

and

$$p'(\mathbf{x},z,t) = \sum_{n=1}^{\infty} p'_n(\mathbf{x},t)\phi_n(\mathbf{x},z). \tag{14}$$

$\mathbf{u}'_n(\mathbf{x},t)$ and $p'_n(\mathbf{x},t)$ are the horizontal baroclinic velocity vector and pressure perturbation modal amplitudes which are computed as

$$\left[\mathbf{u}'_n(\mathbf{x},t), p'_n(\mathbf{x},t)\right] = \frac{1}{H}\int_{-H}^{0} \left[\mathbf{u}'(\mathbf{x},z,t), p'(\mathbf{x},z,t)\right] \phi_n(\mathbf{x},z)\mathrm{d}z. \tag{15}$$

Upon the projection of the linearized hydrostatic equations of motion onto vertical modes, the time-averaged mode n IT energy budget equation is (e.g., Kelly, 2016; Kelly & Lermusiaux, 2016; Kelly et al., 2012; Pan et al., 2021)

$$C_{0n} + C_{mn} = \nabla \cdot \mathbf{F}_n + \Psi_n + D_n, \tag{16}$$

where

$$C_{0n} = \langle p'_n \mathbf{U} \rangle \cdot \nabla(-H)\phi_n\big|_{z=-H}, \tag{17}$$

is the barotropic (mode 0) to baroclinic (mode n) conversion,

$$C_{mn} = \sum_{m=1}^{M} \langle T_{mn} p'_n \mathbf{u}'_m - T_{nm} p'_m \mathbf{u}'_n \rangle \cdot \nabla H \tag{18}$$

is the energy scattering from modes $m > 0$ into mode n due to horizontally varying buoyancy and topography (Zaron et al., 2022). M in Equation 18 is the highest mode resolved (Buijsman et al., 2020; Stewart et al., 2017). The coupling term

$$T_{nm} = \frac{c_n^2}{c_m^2 - c_n^2}\phi_n \phi_m\big|_{z=-H}, \qquad \text{if } m \neq n, \tag{19}$$

and

$$T_{nm} = \frac{1}{2}\left(1 - \phi_n^2\right)\big|_{z=-H}, \qquad \text{if } m = n. \tag{20}$$

The nth mode energy flux

$$\mathbf{F}_n = H\langle p'_n \mathbf{u}'_n \rangle. \tag{21}$$

Ψ_n consists of the energy tendency, the mean flow advection of modal energy, the three-way interactions, and the shear and buoyancy production terms (Pan et al., 2021). However, we estimate Ψ_n to be small in the USWC margin in our numerical simulations (not shown). The modal energy dissipation D_n in Equation 16 is computed as the residual. In addition to dissipation it includes interactions with unresolved modes (i.e., modes $m > M$), modes with higher frequencies, and other processes that lead to local dissipation (Alford & Zhao, 2007).

Following the Griffies and Treguier (2013) criterion that there should be no less than 2π grid cells per wavelength for a wave to be resolved, $M \approx 5$ for the 4-km horizontal resolution simulations. However, this is based on the assumption that the modal structures for the first 5 baroclinic modes are well resolved by the vertical σ-coordinate adopted in the ROMS simulations.

3. Results

3.1. Undecomposed Semidiurnal IT Energetics

The depth-integrated and time-mean (01–30 September 2012) semidiurnal IT energy flux map near the USWC in Figure 1a shows that the Mendocino Escarpment is a hotspot of IT generation. However, only a small amount of the energy flux from this source reaches the USWC margin. This is because the USWC margin is nearly parallel to the energy flux beams from the Mendocino Escarpment. With the inclusion of remote IW forcing at the open boundaries, the semidiurnal IT energy flux field near the USWC becomes more complex (Figure 1b). The remote ITs not only increase the energy levels near the USWC, they also reach the continental margin. Remote IT beams impinge on the USWC margin at 35°N, 38°N, and 45°N. We show the spatial maps for September because the magnitude of the remote semidiurnal IT energy fluxes reaching the continental margin is highest during this month (see next section).

Although the modulation of the local IT generation by the remote ITs varies spatially in the USWC margin (Figure 2), the monthly-mean and area-integrated barotropic-to-baroclinic energy conversion rates (C) in the

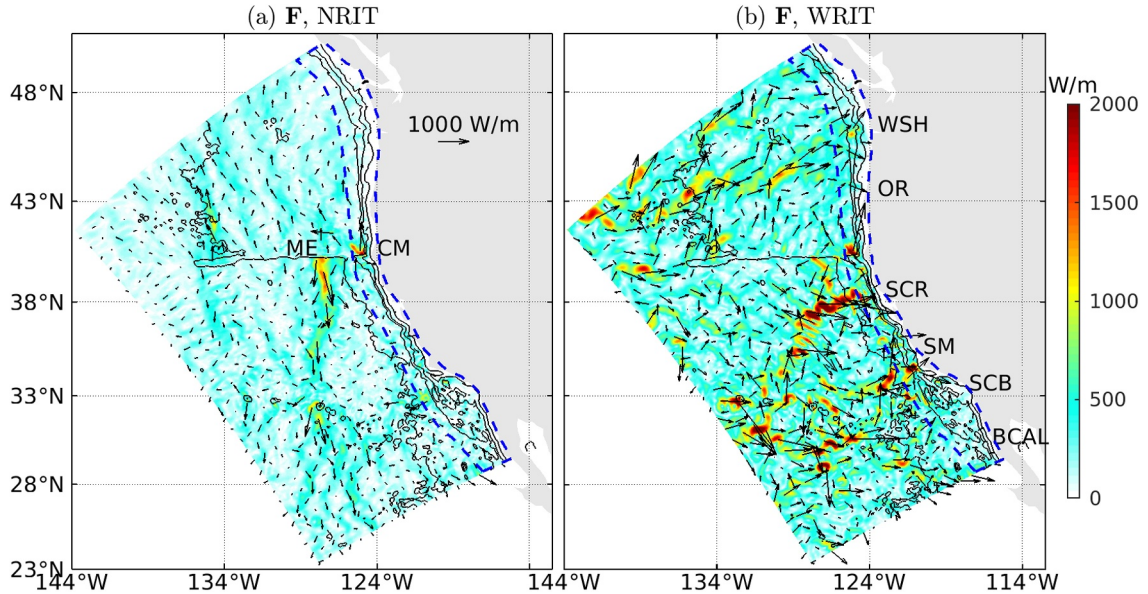

Figure 1. Depth-integrated and time-mean (01–30 September 2012) semidiurnal baroclinic energy fluxes near the U.S. West Coast for (a) NRIT, a simulation without remote internal wave (IW) forcing, and (b) WRIT, a simulation with remote IW forcing at the open boundaries. In (a) and (b), ME is Mendocino Escarpment, CM is Cape Mendocino, BCAL is Baja California, SCB is Southern California Bight, SM is Santa Maria basin, SCR is Sacramento basin, OR is Oregon, and WSH is Washington. The black curves in (a) and (b) are the 200, 1,000, 2,000, and 4,000 m seafloor depth contours while the dashed blue polygon marks the continental margin. Here, we define the continental margin as the region extending from the shoreline to the foot of the continental slope (3,500 m isobath for BCAL, SCB, SM, and SCR, 3,000 m for OR, and 2,500 m for WSH).

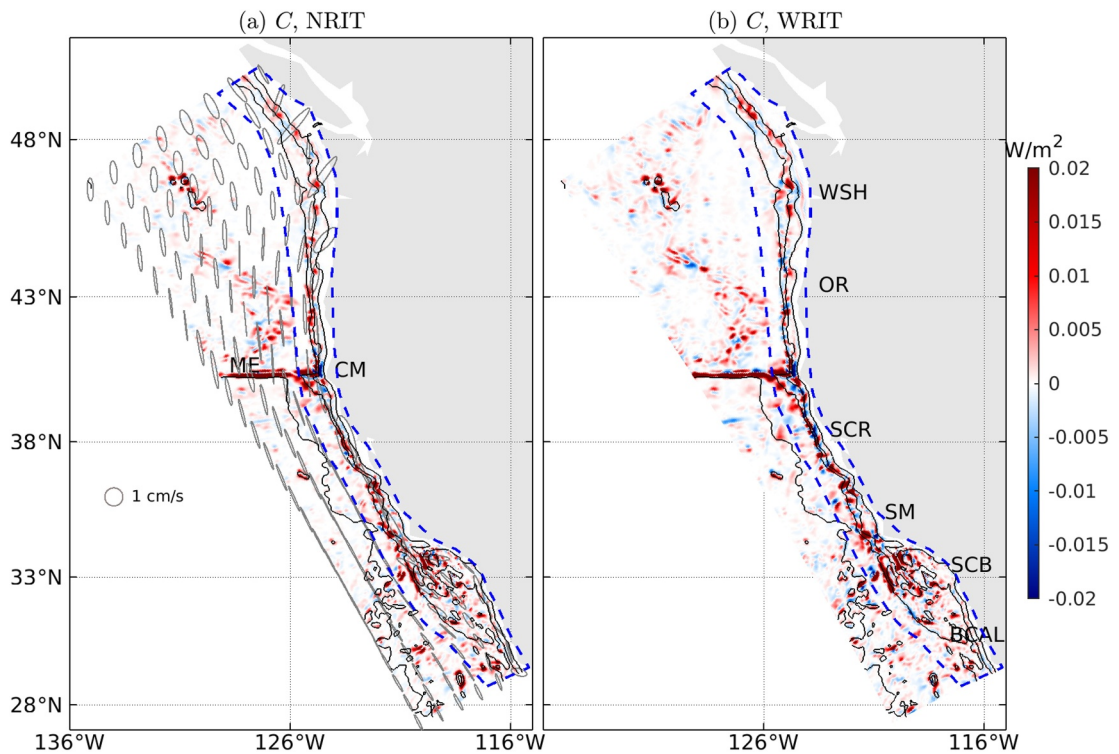

Figure 2. Time-mean (01–30 September 2012) semidiurnal barotropic-to-baroclinic energy conversion near the U.S. West Coast for (a) NRIT, a simulation without remote internal wave (IW) forcing, and (b) WRIT, a simulation with remote IW forcing at the open boundaries. The gray ellipses in (a) are the M_2 barotropic tidal current ellipses. The M_2 tides are the major semidiurnal barotropic tides near the USWC. The black curves in (a) and (b) are the same depth contours as in Figure 1 and the dashed blue polygon marks the continental margin. ME, CM, WSH, OR, SCR, SM, SCB and BCAL in (a) and (b) are defined in Figure 1 caption.

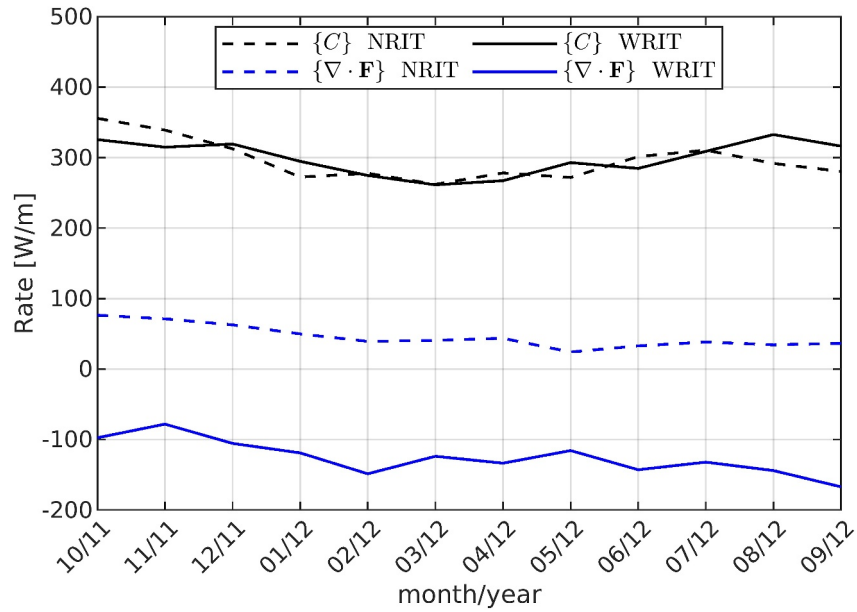

Figure 3. Monthly-mean and area-integrated semidiurnal barotropic-to-baroclinic energy conversion ($\{C\}$, black curves) and energy flux divergence ($\{\nabla \cdot \mathbf{F}\}$, blue curves) in the USWC continental margin for the simulations without (NRIT, dashed) and with (WRIT, solid) remote internal wave forcing. The area-integrated C and $\nabla \cdot \mathbf{F}$ estimates are normalized by the total length of the coastline (~2,644 km). {..} represents area-integration.

NRIT and WRIT solutions are similar throughout the year (black curves, Figure 3). However, the conversion estimates in Figure 3 (<1 GW; 0.38 kW/m length of coastline) indicate that the USWC margin is not a strong IT generation site compared to other continental shelf regions, for example, the Amazon shelf (3.3 kW/m; Tchilibou et al., 2022), Bay of Biscay (10 kW/m, Gerkema et al., 2004), and Gulf of Maine (6 kW/m; Schindelegger et al., 2022). This is because the surface tidal velocities near USWC are mainly along the isobaths of large topographic features (Figure 2a (gray ellipses), Kelly et al., 2012; Nash et al., 2007). Moreover, our estimates may be underestimated because the topographic features in the USWC margin may not be fully resolved with the 4-km grid resolution (Buijsman et al., 2020; Jachec et al., 2007). Unlike conversion, the area-integrated flux divergence $\nabla \cdot \mathbf{F}$ in the USWC margin for the two simulations varies significantly (blue curves, Figure 3). Area-integrated $\nabla \cdot \mathbf{F}$ in the margin is > 0 throughout the 1-year period in the NRIT solution. This implies a net radiation of semidiurnal IT energy fluxes out of the USWC margin throughout the year. A significant amount of which also leaves through the northern and southern boundaries. In contrast, semidiurnal IT energy fluxes radiate into the USWC margin in the WRIT solution because the area-integrated $\nabla \cdot \mathbf{F}$ is < 0 for all the months.

3.2. Directionally Decomposed IT Energy Fluxes

The directionally decomposed IT energy flux maps in Figure 4 confirm that the remote energy fluxes exceed those radiating out of the USWC margin in the WRIT solution. Near Oregon, Washington, and Central California (i.e., the Sacramento and the Santa Maria basins) where the net energy flux in the WRIT simulation is into the continental margin (Figure 1b), onshore energy fluxes are stronger than the offshore energy fluxes. Nonetheless, IT energy fluxes of $\mathcal{O}$(1,000) W/m radiate out of the USWC margin from the Southern California Bight, the Sacramento Basin and also from the Cape Mendocino (Figure 4b). Note that the cross-term energy fluxes (not shown) are small in the USWC margin compared to the onshore and offshore energy fluxes.

The temporal variability in the monthly-mean along-shore integrated onshore and offshore propagating IT energy fluxes at the foot of the continental slope for the NRIT and WRIT simulations is illustrated in Figure 5. For the NRIT simulation, the along-shore integrated onshore energy flux is 138.2 ± 9.4 W/m. Sources of this onshore energy flux in the NRIT simulation are the Mendocino Escarpment and other nearby rough topographic features. However, the along-shore integrated onshore energy flux in the WRIT simulation is about 3 times larger than in the NRIT simulation. Also, the temporal variability in the onshore energy fluxes in the WRIT simulation is greater than in the NRIT simulation, with a minimum value of 313 W/m in October 2011 and a maximum value of 474 W/

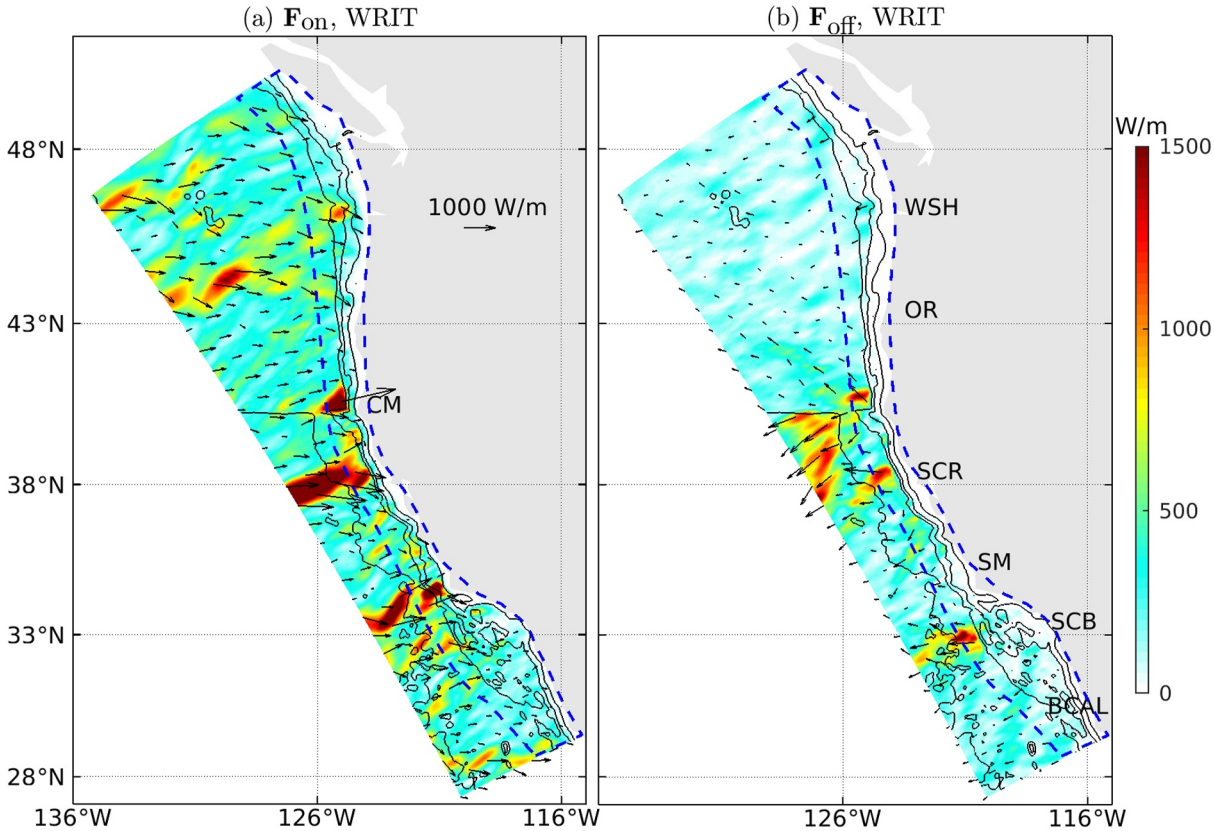

Figure 4. Depth-integrated and time-mean (01–30 September 2012) (a) onshore and (b) offshore propagating semidiurnal internal tide energy fluxes for the WRIT simulation near the USWC. The black curves in (a) and (b) are the same depth contours as in Figure 1 and the dashed blue polygon marks the continental margin. CM, WSH, OR, SCR, SM, SCB, and BCAL in (a) and (b) are defined in Figure 1 caption.

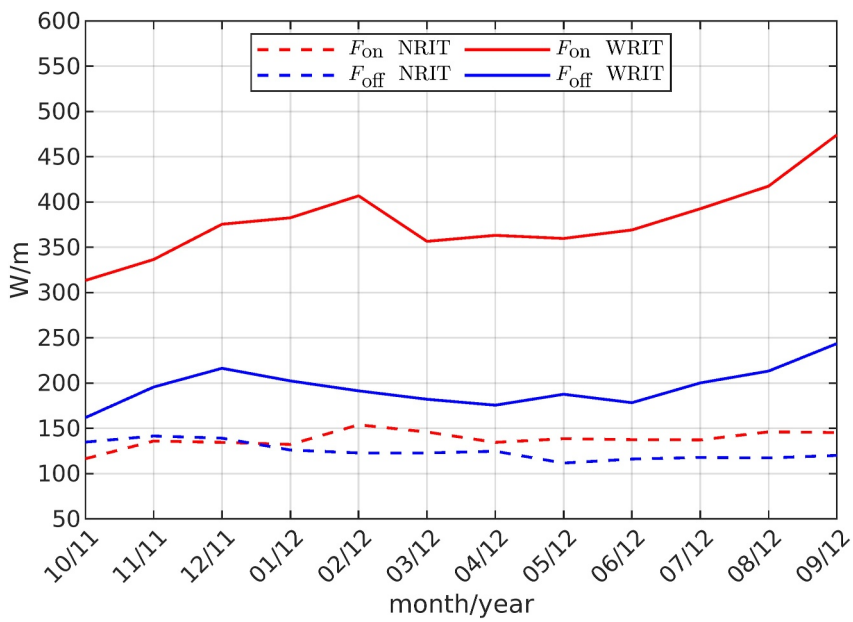

Figure 5. Monthly-mean and along-shore integrated perpendicular onshore (red curves) and offshore (blue curves) semidiurnal internal tide energy fluxes at the foot of the USWC continental slope for the simulations without (NRIT, dashed) and with (WRIT, solid) remote internal wave forcing. The along-shore integrated onshore and offshore fluxes are normalized by the total length of the coastline (~2,644 km).

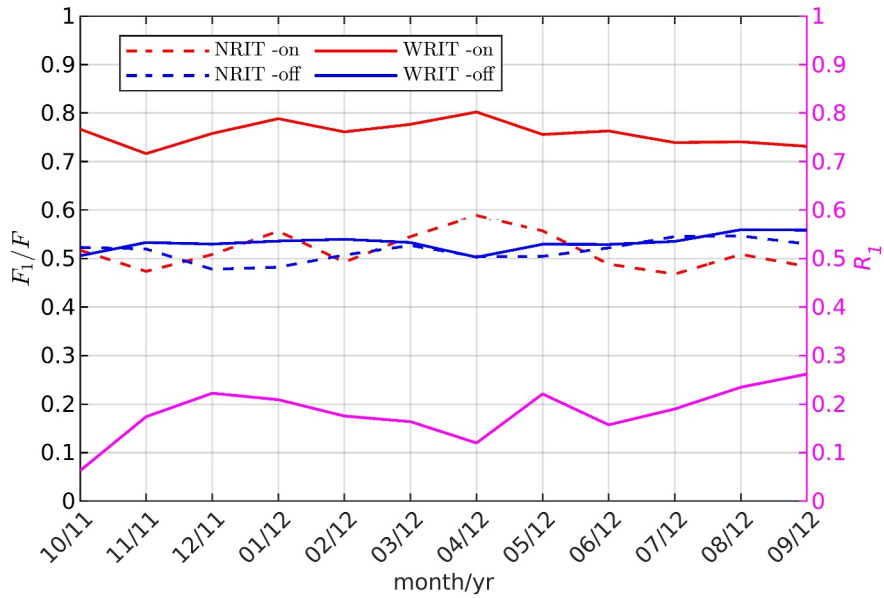

Figure 6. Onshore (red curves) and offshore (blue curves) mode-1 energy flux as a fraction of the total flux (F) at the foot of the continental slope for the simulations without (NRIT, dashed) and with (WRIT, solid) remote internal wave forcing. The magenta curve and the right axis label represent the remote mode-1 semidiurnal internal tide reflectivity of the continental margin (Equation 22).

m in September 2012. The along-shore integrated offshore energy fluxes at the foot of the continental slope are similar in magnitude to the onshore energy fluxes in the NRIT simulation throughout the year. Although the local generation in the USWC margin is similar in both the NRIT and WRIT simulations (Figure 3), the offshore energy fluxes in the WRIT solution are larger than the offshore fluxes in the NRIT solution. This implies that a significant amount of the remote IT signals is reflected by the continental margin in the WRIT simulation. For example, the increase of F_{on} after June 2012 coincides with an increase in F_{off} (Figure 5), indicating an increase in reflected energy.

3.3. Mode-1 IT Reflectivity

At the foot of the USWC continental slope, modes 1–5 constitute ~99% of the onshore and offshore semidiurnal IT energy fluxes for both the NRIT and WRIT simulations throughout the year (not shown). However, the modal composition in these simulations differ (Figure 6). In the NRIT simulation, approximately half of the onshore and offshore energy fluxes is in mode-1. The remaining half of the energy fluxes is in modes 2–5 and higher. While mode-1 also constitutes approximately half of the offshore energy fluxes at the foot of the continental slope in the WRIT simulation, about 72%–80% of the onshore energy flux is in mode-1. Because the majority of the remote energy fluxes is in mode-1, our focus in the remaining part of this paper will be on the fate of the remote mode-1 semidiurnal ITs.

Based on our finding that the area-integrated semidiurnal band barotropic-to-baroclinic conversion rates in the USWC margin in the NRIT and WRIT simulations are similar (Figure 3), we estimate the mode-1 reflectivity of the continental margin as

$$R_1 = \frac{F_{1,\text{off}}^{\text{WRIT}} - F_{1,\text{off}}^{\text{NRIT}}}{F_{1,\text{on}}^{\text{WRIT}} - F_{1,\text{on}}^{\text{NRIT}}}, \tag{22}$$

where $F_{1,\text{on}}^{\text{NRIT}}$, $F_{1,\text{on}}^{\text{WRIT}}$, $F_{1,\text{off}}^{\text{NRIT}}$ and $F_{1,\text{off}}^{\text{WRIT}}$ are the monthly-mean and along-shore integrated perpendicular mode-1 onshore and offshore energy fluxes at the foot of the continental slope in the NRIT and WRIT simulations. Here, $F_{1,\text{off}}^{\text{WRIT}} - F_{1,\text{off}}^{\text{NRIT}}$ is the reflected energy flux, F_{r}, and $F_{1,\text{on}}^{\text{WRIT}} - F_{1,\text{on}}^{\text{NRIT}}$ is the remote incident energy flux, F_{in} (see Section 2.3). The mode-1 semidiurnal IT reflectivity of the USWC margin is 18.2 ± 5.4% (magenta curve;

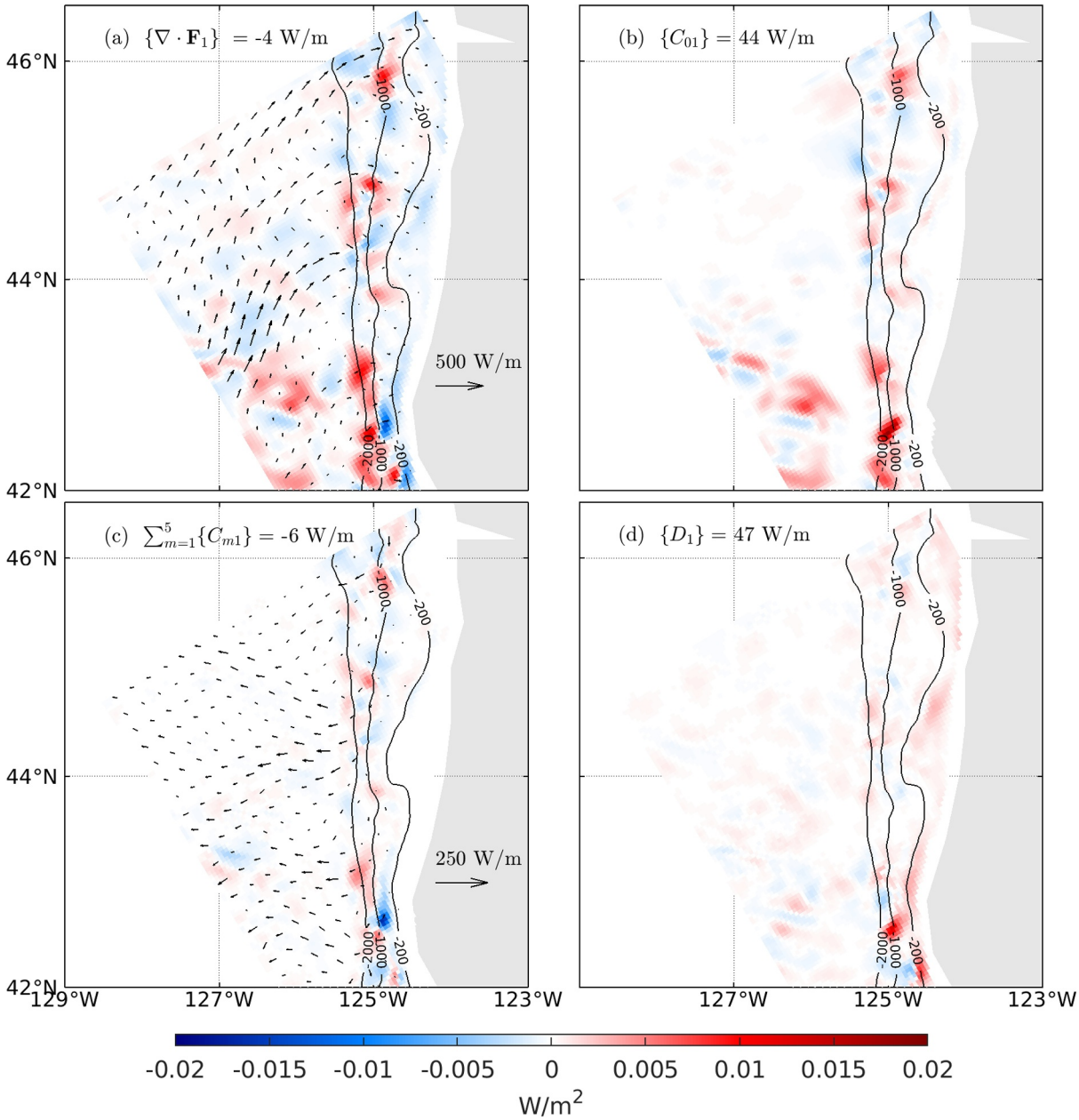

Figure 7. Time-mean (01–30 September 2012) mode-1 internal tide (IT) (a) energy flux divergence, (b) barotropic-to-baroclinic tide energy conversion, (c) energy scattering to modes 2–5, and (d) dissipation near the Oregon coast for the simulation without remote internal wave forcing (NRIT). Note that we do not include the spatial map for the fourth term of the energy balance in Equation 16, that is, Ψ_1. {..} in (a)–(d) represents area-integrated values in the continental margin normalized by the length of Oregon coastline (~487 km). The vectors in (a) are the onshore propagating mode-1 IT energy flux vectors and those in (c) are the offshore propagating modes 2–5 energy flux vectors. The black curves in (a)–(d) are the 200, 1,000, and 2,000 m depth contours.

Figure 6). The minimum (6%) and maximum (26%) R_1 estimates occur in October 2011 and September 2012 in which the minimum and maximum onshore fluxes in the WRIT simulation also occur, respectively (Figure 5). The fate of the remaining ~80% of the remote mode-1 semidiurnal IT energy fluxes is investigated in the following sections.

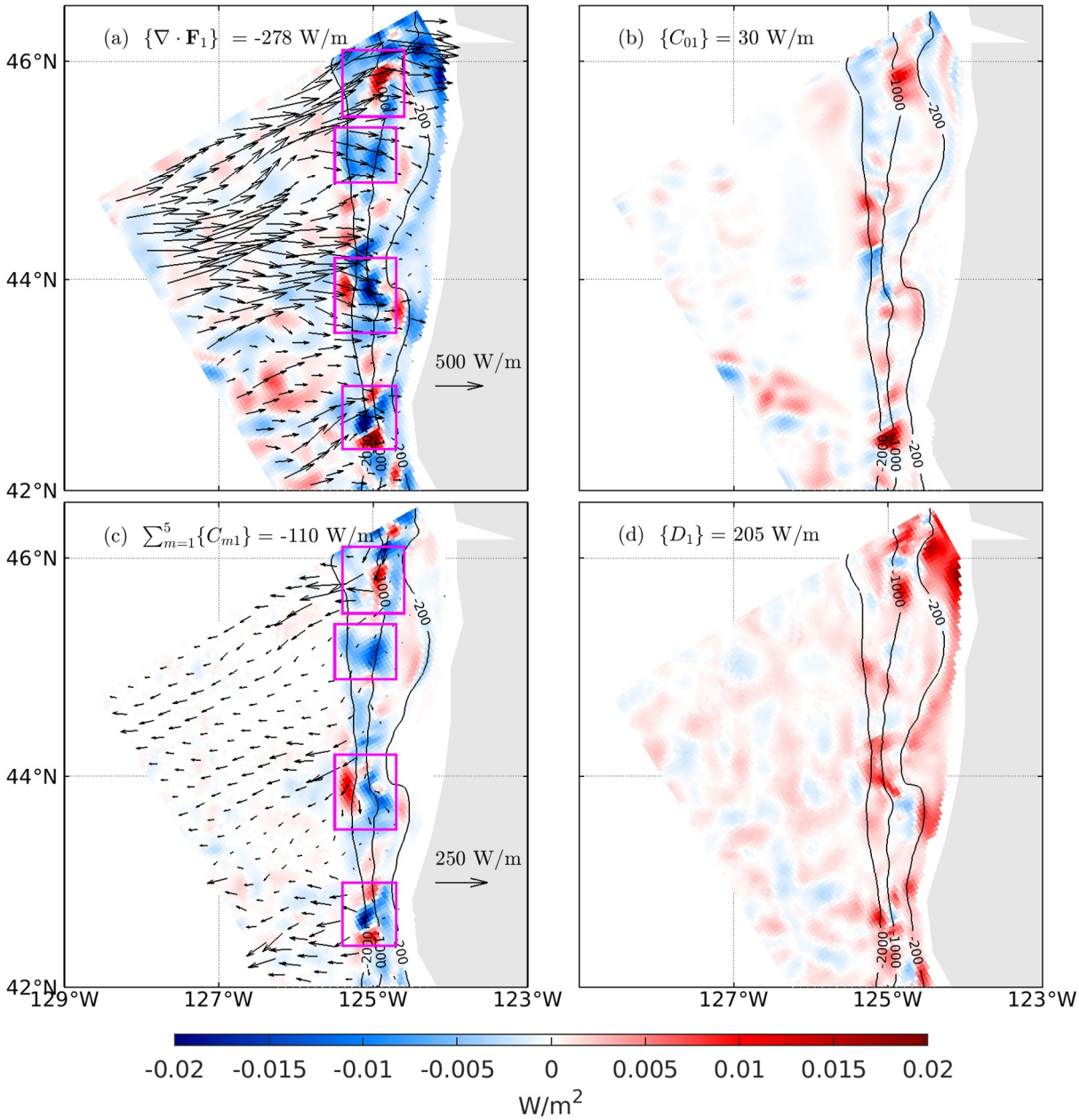

Figure 8. Same as Figure 7 but for the simulation with remote internal wave forcing (WRIT). The magenta boxes are discussed in the text.

3.4. Mode-1 IT Energy Balance off the Oregon Coast

As an illustration, we discuss the increased mode-1 IT energy scattering and dissipation along the Oregon coast due to the remote ITs (Figures 7 and 8). For the same reason as explained in Section 3.1, the energy terms discussed here are for the month of September.

The time-mean (01–30 September 2012) spatial maps of the energy balance terms in Equation 16 for mode-1 semidiurnal ITs near the Oregon coast for the NRIT solution are shown in Figure 7. Although the energy flux divergence agrees with the barotropic-to-baroclinic conversion in many locations (Figures 7a and 7b), the onshore mode-1 energy fluxes are greater than those radiating out of the continental margin ($\{\nabla \cdot \mathbf{F}\} = -4$ W/m; Figure 7a). The non-locally generated mode-1 energy fluxes are most likely from the Mendocino Escarpment. Approximately 13.6% $\left(\frac{6 \text{ W/m}}{44 \text{ W/m}}\right)$ of the power input into mode-1 energy from the barotropic tides is scattered into

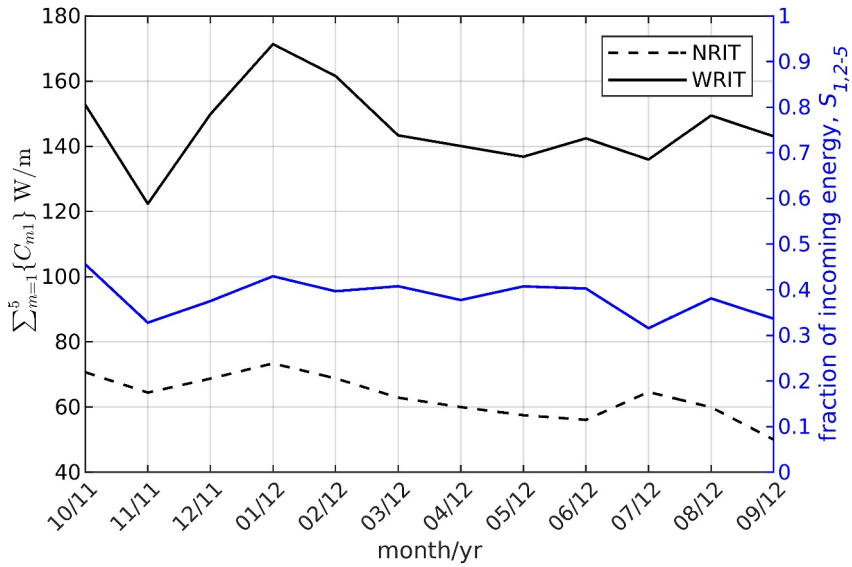

Figure 9. Monthly-mean and area-integrated internal tide (IT) energy scattering rate from mode-1 to modes 2–5 in the USWC margin for the simulations without (NRIT, dashed black curve) and with remote internal wave forcing (WRIT, solid black curve). The blue curve and the right axis label represent the fraction of the remote mode-1 IT energy flux scattered to modes 2–5 (Equation 23). The area-integrated scattering estimates are normalized by the total length of the coastline (~2,644 km).

modes 2–5 (Figure 7c). The net amount of mode-1 IT energy dissipation in the Oregon continental margin is 45 W/m (Figure 7d), with a significant amount of it occurring over seafloor depths <200 m.

Unlike in the NRIT solution, the spatial maps of barotropic-to-baroclinic conversion and energy flux divergence look different in the WRIT solution (Figures 8a and 8b). In addition to a decrease in $\{C_{01}\}$ by 31.8% $\left(\frac{30-44\ \text{W/m}}{44\ \text{W/m}}\right)$, the area-integrated mode-1 energy flux divergence is more negative in the WRIT solution ($\{\nabla \cdot \mathbf{F}\} = -278$ W/m; Figure 8b) than in the NRIT solution. While some of the remote mode-1 energy flux is reflected back into the open ocean, the remaining is scattered into modes 2–5 ($C_{2-5,1}$) and dissipated in the continental margin. With remote IW forcing, the mode-1 to higher mode scattering ($\{C_{2-5,1}\}$) in the Oregon continental margin is ~18 times $\left(\frac{110\ \text{W/m}}{6\ \text{W/m}}\right)$ greater (Figure 8c) than in the NRIT solution. Hotspots of mode-1 energy scattering to higher modes, that is, negative $C_{2-5,1}$, in the continental margin in Figure 8c, coincide with regions of negative mode-1 flux divergence in Figure 8a (see magenta boxes in Figures 8a and 8c). Although some of the scattered mode-1 energy would likely contribute to onshore fluxes of modes 2–5, we observe stronger mode 2–5 fluxes propagating offshore in the WRIT solution than in the NRIT solution (black arrows; Figures 7c and 8c). The strong correlation ($r \approx 0.7$) between the monthly-mean time series of along-shore integrated offshore propagating mode 2–5 fluxes ($F_{2\text{-}5,\text{off}}$) and $\{C_{2-5,1}\}$ (not shown) confirms that the local barotropic tide conversion to modes 2–5 ($C_{0,2-5}$) is not responsible for the bulk of these offshore fluxes in the WRIT simulation. Lastly, we estimate that 4.4 $\left(\frac{205\ \text{W/m}}{47\ \text{W/m}}\right)$ times more mode-1 energy dissipation occurs in the Oregon continental margin in the WRIT solution than in the NRIT solution (Figure 8d).

As will be shown in the following sections, with remote IW forcing we find higher mode-1 IT energy scattering and dissipation throughout the year, not only near the Oregon coast, but also in other regions in the USWC margin.

3.5. Mode-1 IT Energy Scattering

The monthly averages of the area-integrated mode-1 IT energy scattered to modes 2–5 in the USWC margin for both the NRIT and WRIT simulations are shown in Figure 9. In the NRIT solution, 63.1 ± 6.8 W/m of mode-1 energy is scattered to modes 2–5. However, throughout the year, the amount of mode-1 energy scattered to higher modes in the USWC margin increases in the WRIT solution relative to the NRIT solution (89.8%–186.0%

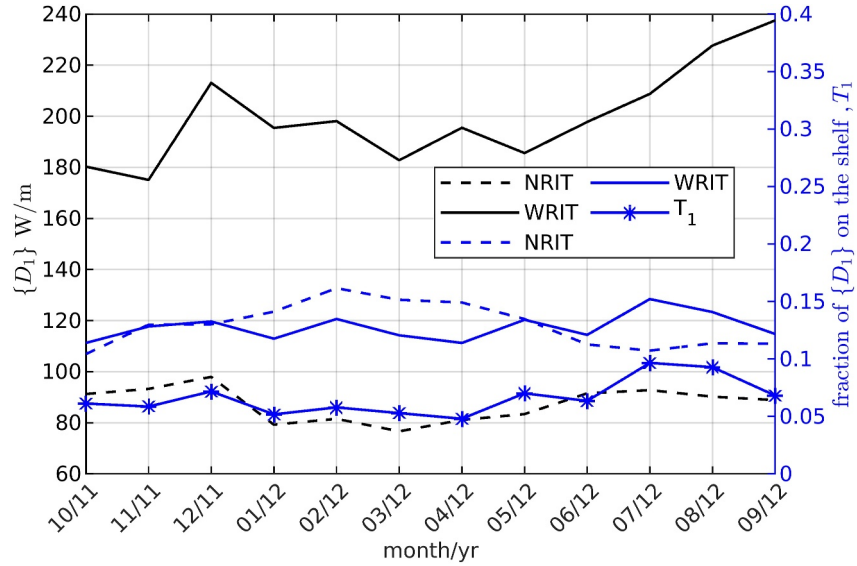

Figure 10. Monthly-mean and area-integrated mode-1 internal tide (IT) dissipation $\{D_1\}$ in the USWC margin for simulations without (NRIT, dashed black curve) and with (WRIT, solid black curve) remote internal wave forcing. The blue curves and the right axis label represent the fractions of D_1 that occur in the continental shelf ($H \leq 125$ m) in the NRIT (dashed) and WRIT (solid) simulations. The solid blue curve with * markers represents the remote mode-1 IT transmissivity onto the continental shelf, T_1 (Equation 24). The area-integrated dissipation estimates are normalized by the total length of the coastline (~2,644 km).

increase). The maximum amount of mode-1 energy scattered in both the WRIT and NRIT simulations occurs in January. We attribute the presence of a weaker pycnocline stratification to the observed peaks in scattering (Gerkema, 2001; Tchilibou et al., 2022). Unlike in the NRIT solution, whose monthly mean $\{C_{2-5,1}\}$ estimates show an overall declining trend, no clear trend in the monthly mean $\{C_{2-5,1}\}$ estimates exists in the WRIT solution.

Also included in Figure 9 is the fraction of the remote mode-1 energy fluxes scattered to modes 2–5 for each month. We compute the remote mode-1 IT energy scattering fraction in the USWC margin as

$$S_{1,2-5} = \frac{\{C^{\mathrm{WRIT}}_{2-5,1}\} - \{C^{\mathrm{NRIT}}_{2-5,1}\}}{F^{\mathrm{WRIT}}_{1,\mathrm{on}} - F^{\mathrm{NRIT}}_{1,\mathrm{on}}}, \tag{23}$$

where $\{C^{\mathrm{NRIT}}_{2-5,1}\}$ and $\{C^{\mathrm{WRIT}}_{2-5,1}\}$ are the monthly-mean and area-integrated mode-1 IT energy scattered to modes 2–5 in the NRIT and WRIT solutions, respectively. In the USWC margin, the fraction of the remote mode-1 IT energy scattered to modes 2–5 via interactions with a horizontally varying topography and stratification is nearly uniform throughout the year with $S_{1,2-5} = 38.5 \pm 4.2\%$.

3.6. Mode-1 IT Energy Dissipation

Across all months, the mode-1 energy dissipation in the USWC margin increases with remote IW forcing (Figure 10). Integrating the dissipation in the continental margin, 87.3 ± 6.7 W/m of mode-1 energy is dissipated in the NRIT solution and 199.8 ± 19.0 W/m in the WRIT solution. In the NRIT solution, the time series of the monthly averages of the area-integrated dissipation have a strong correlation ($r = 0.76$) with those of the local barotropic-to-baroclinic conversion (Figure 3). This implies that most of the dissipation in the USWC margin in the NRIT solution is due to the locally generated mode-1 IT energy. However, in the WRIT solution, there is a strong correlation ($r = 0.85$) between the time series of the monthly averages of the area-integrated dissipation and the along-shore integrated onshore energy fluxes (not shown).

The fraction of the dissipation that occurs on the shelf ($H \leq 125$ m) in both the NRIT (12.9 ± 1.9%) and WRIT (12.8 ± 1.2%) simulations are similar (Figure 10). This suggests that overall, no drastic modification to the

stratification profiles near the USWC takes place in the presence of remote ITs. Hall et al. (2013) found the fraction of incident IW energy transmitted onto the shelf to be dependent on the depth structure of the stratification. Assuming that all remote IT energy that propagates onto the continental shelf is dissipated, we compute the fraction of the remote mode-1 IT energy transmitted onto the shelf as

$$T_1 = \frac{\{D_{1,\text{shelf}}^{\text{WRIT}}\} - \{D_{1,\text{shelf}}^{\text{NRIT}}\}}{F_{1,\text{on}}^{\text{WRIT}} - F_{1,\text{on}}^{\text{NRIT}}}, \tag{24}$$

where $\{D_{1,\text{shelf}}^{\text{NRIT}}\}$ and $\{D_{1,\text{shelf}}^{\text{WRIT}}\}$ are the monthly-mean and area-integrated mode-1 IT energy dissipation estimates in the continental shelf in the NRIT and WRIT solutions, respectively. Overall, 6.6 ± 1.5% of the remote mode-1 IT energy is transmitted onto and dissipated on the USWC continental shelf (Figure 10). However, because of the grid resolution, we note that the transmissivity estimates may not be accurate as there are few grid cells (an average of 6) along the continental margin for $H \leq 125$ m.

4. Discussion

4.1. Along-Shore Variability in Mode-1 IT Reflectivity, Scattering, and Transmissivity

Based on the amount of remote semidiurnal IT energy flux that reaches the USWC margin through its western boundary (0.24 ± 0.03 kW/m), we conclude that the bulk of the IT energy generated at Hawaii dissipates in the open ocean. Out of the 3.93 kW/m of M_2 IT energy (modes 1–5) generated at Hawaii (155–180°W; Buijsman et al., 2020), 6% $\left(\frac{0.24}{3.93}\right)$ reaches the USWC margin. While a fraction of the remote mode-1 semidiurnal IT energy fluxes reaching the USWC margin is reflected back to the open ocean ($R_1 \approx 20\%$), the remaining is scattered to higher modes (modes 2–5, $S_{1,2-5} \approx 40\%$), transmitted onto the shelf ($T_1 \approx 7\%$) and dissipated on the continental slope (≈33%). These estimates are comparable to the regional averages of Kelly et al. (2013) for the East Pacific basin margin ($R_1 = 30\%$, $S_{1,2-16} = 60\%$, $T_1 = 10\%$). However, Kelly et al. (2013) ignored dissipation, which is a non-negligible contribution. Taking similar approaches as in Sections 3.3, 3.5, and 3.6 but integrating over the different basins indicated in Figure 1b, we look into the spatial variability in what follows.

The yearly averages of energy fluxes in Figure 11a indicate that the Sacramento basin (SCR) receives the highest amount of remote mode-1 semidiurnal IT energy (≈400 W/m) of all the USWC basins. The lowest amount of 170 W/m is recorded for the Washington margin (WSH). For the remaining regions along the USWC, the amount of remote mode-1 energy flux varies between 260 and 345 W/m. Although the standard deviations over the yearly averages are significant for each basin (≈17–38% of the annual mean; whiskers in Figure 11a), we find no clear seasonal variability. Hence, we do not observe clear seasonal variations in the R_1, $S_{1,2-5}$ and T_1 estimates either. The strength of the remote IT beams for each segment do not only vary in time but also their incidence angles (not shown). This is likely due to interactions with the spatio-temporally varying mesoscale structures between Hawaii and the USWC (Rainville & Pinkel, 2006; Zaron & Egbert, 2014). Overall, throughout the year the angle of incidence for the remote IT beams for all the segments varies between ±36° with respect to the shoreline normal.

Along the USWC, mode-1 reflectivity is modest everywhere ($R_1 < 20\%$, Figure 11b) except for the SCR margin whose reflectivity averages 31% and is as high as 49% in September. A plausible explanation is that, of all the segments, the SCR margin has the largest fraction of area where the slope is supercritical (Figures 11c and 12). Moreover, the area with supercritical slope is the most continuous and the least patchy as compared to the other segments (Figure 12). Hence, this makes the SCR margin a more effective IT reflector than the other segments. Furthermore, we observe that the incidence angle (β) influences mode-1 reflectivity for the SCR margin. In September, during which the maximum reflectivity is recorded for SCR, the incident beams are nearly perpendicular to the shoreline ($\beta = 6°$, Figure 4a), whereas, the incident ITs are more oblique during other months. For the other regions in the USWC margin, there exists little to no correlation between β and R_1. We attribute this to the abundance of sub(near)-critical slope areas in these segments.

In contrast to the reflectivity, the fraction of the remote mode-1 energy scattered to higher modes is low for SCR (8%) and high for the remainder of the USWC margin ($S_{1,2-5} \approx$ 33–48%, Figure 11b). It's not surprising that we observe appreciable IT energy scattering in the USWC margin, because it features rough and near-critical bathymetry. While we record high roughness (H_{rms}) values for the SCR margin, we do not observe significant mode-1 energy scattering to higher modes there. However, we find the areas with high

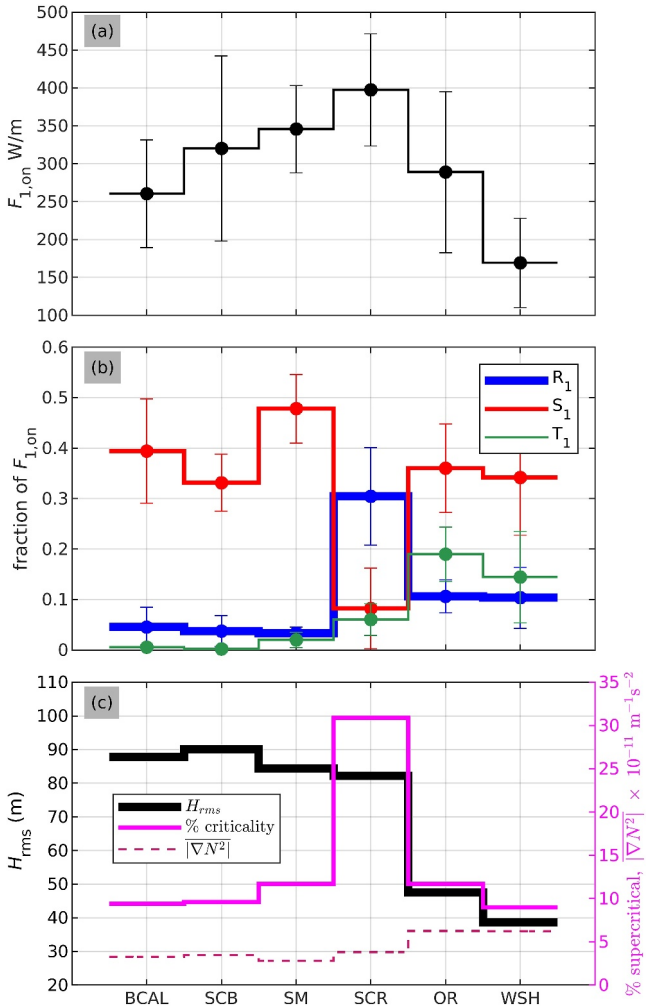

Figure 11. (a) The remote mode-1 semidiurnal internal tide energy flux, (b) the fraction of the remote mode-1 energy flux that is reflected (blue curve), scattered (red curve), and transmitted onto the continental shelf (green curve), and (c) spatially averaged topographic roughness (H_{rms}, black curve), depth-averaged yearly-mean buoyancy gradient $\overline{|\nabla N^2|}$ (dashed, magenta curve), and % of the margin that is supercritical (solid, magenta curve) along the USWC. The filled circles in (a) and (b) represent the yearly averages, while the whiskers depict one standard deviation from the mean. The topographic roughness at cell (i, j) is computed as $H_{rms,(i,j)} = \sqrt{\left[(H_{i,j} - H_{i+1,j})^2,\ (H_{i,j} - H_{i-1,j})^2,\ (H_{i,j} - H_{i,j+1})^2,\ (H_{i,j} - H_{i,j-1})^2\right]}$, where [..] represents the mean over the squares of the differences in seafloor depths with the neighboring cells. $\overline{|\nabla N^2|} = \frac{1}{H}\int_{-H}^{0}\sqrt{\left(\partial N^2/\partial x\right)^2 + \left(\partial N^2/\partial y\right)^2}\,\mathrm{d}z$. BCAL, SCB, SM, SCR, OR and WSH are defined in Figure 1.

roughness on the SCR continental slope to be supercritical. Thus indicating that the SCR slope is an IT reflector and not a good scatterer. Furthermore, although the Oregon-Washington (OR-WSH) margins have smaller H_{rms} compared to the BCAL, SCB and SM margins, a similar fraction of the remote mode-1 energy is scattered there. The ocean near the OR-WSH coast has a more spatially heterogeneous buoyancy field (Figure 11c, dashed-magenta curve). We hypothesize this may compensate for the smaller roughness because the topographic scattering coupling terms depend on the horizontal gradients in both seafloor depth and stratification (Kelly, 2016; Zaron et al., 2022).

The OR-WSH margins do not only have small areas with supercritical slope, they also have milder slopes and stronger near-surface stratification (not shown) compared to the other regions in the USWC margin. These factors allow a higher fraction of the incident ITs to be transmitted onto the continental shelves off the OR-WSH coasts (Figure 11b, Hall et al., 2013; S. Wang et al., 2018). Freshwater plumes from the Columbia river into the OR-WSH continental shelves are most likely responsible for the stronger near-surface stratification (Hickey et al., 2005; Mazzini et al., 2015). In the NRIT and WRIT simulations, river-runoff forcing was applied as surface precipitation using a Gaussian distribution over a distance of 150 km from the coast (Renault et al., 2021). On average, ∼17% of the remote mode-1 energy is transmitted and available for mixing on the OR-WSH shelves, whereas, <10% of the remote mode-1 IT energy is transmitted onto the shelf for the coastal segments to the south. Osborne et al. (2011) found a similar fraction (17.2%) of M_2 IT energy generated on the Oregon slope that is transmitted onto the shelf.

4.2. Impact of the Remote ITs on Stratification

Prompted by our finding in Section 3.6, we examine whether the increased energy flux into the continental margin due to the remote ITs causes changes in the stratification. For this purpose, we quantify the changes in the subsurface temperature, buoyancy frequency, vertical mixing diffusivity, and temperature advection in the margin between the NRIT and WRIT solutions (Figure 13). Although the changes in stratification are due to changes in both temperature and salinity, we only discuss temperature changes in this paper.

In the NRIT simulation, the downward tilt of the isotherms toward the slope at depth (Figure 13a) can be attributed to the northward flowing California Undercurrent (Checkley & Barth, 2009). In contrast, in the surface layers the isotherms are tilting upwards toward the coast (inset; Figure 13a), which is an indication of coastal upwelling. This is due to the prevailing upwelling favorable southward winds (Gan & Allen, 2005). With remote IT forcing, the largest temperature differences ($\pm\mathcal{O}(0.1)$ °C) between the NRIT and WRIT solutions are observed in the first 300 m (Figure 13), with a resultant cooling at the surface and warming at depth (inset; Figure 13b). Also, there is evidence of heat redistribution for $z < -300$ m, but the changes in temperature are one order of magnitude smaller ($\pm\mathcal{O}(0.01)$ °C). A strong positive correlation coefficient of 0.7 between the monthly averaged time series of the remote IT energy fluxes (Figure 5) and the root-mean-square (rms) differences in temperature over the slope (Figure 13h), confirms that the heat redistribution we observe in the USWC margin is modulated by the remote ITs. Overall, the rms difference in temperature between the two simulations is 0.04 ± 0.02°C for the entire water column over the slope and 0.05 ± 0.02 for the surface 300 m.

The along-shore spatial averages of the buoyancy frequency N^2 in the NRIT solution in Figure 13c indicate that the stratification near the USWC is stronger in the upper 130 m, with the thermocline located at approximately

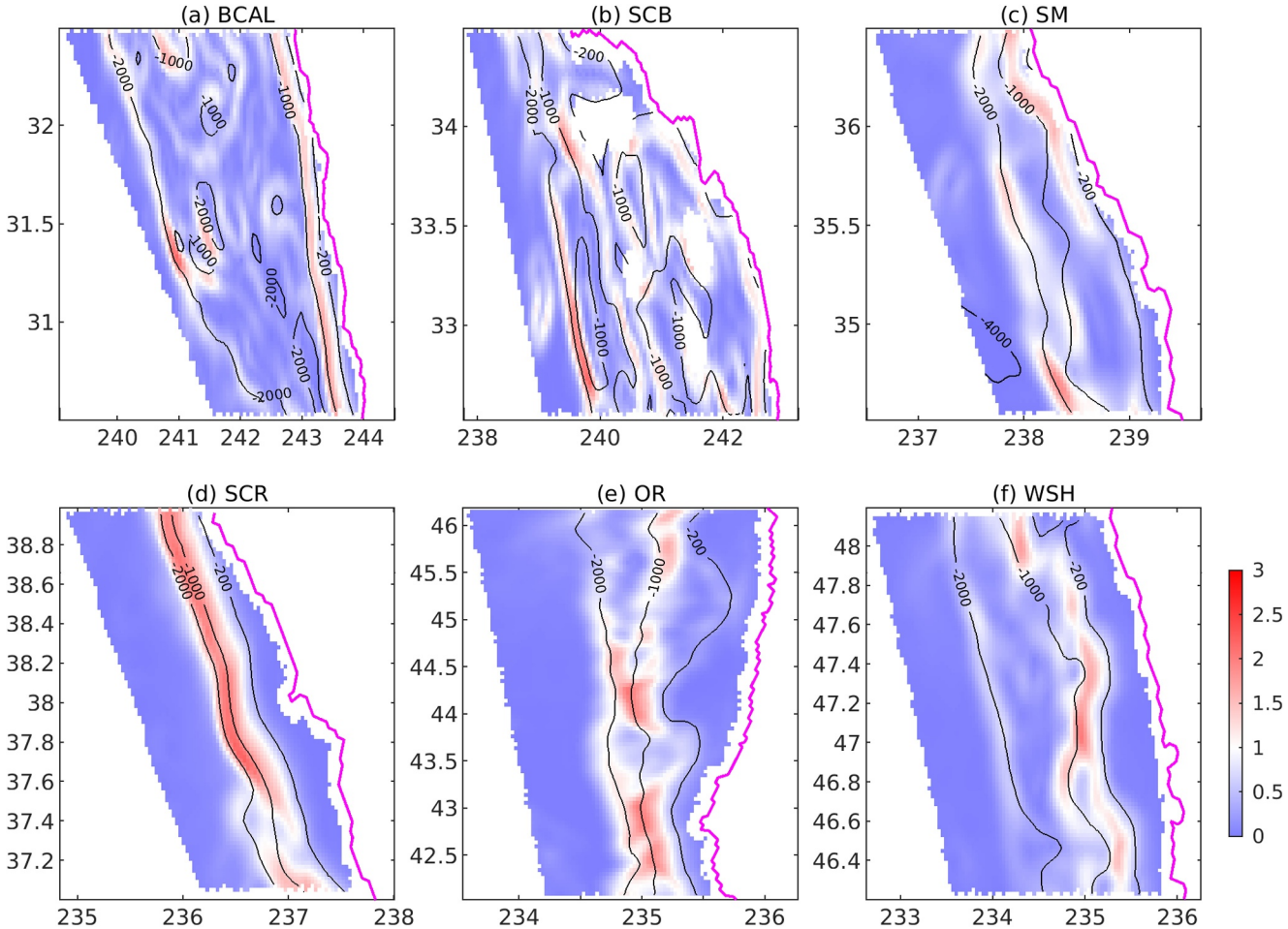

Figure 12. Criticality parameter γ computed using the mean bottom stratification for the whole year for (a) BCAL, (b) SCB, (c) SM, (d) SCR, (e) OR, and (f) WSH continental margins. $\gamma = |\nabla H|/s$, where the bathymetry gradient $|\nabla H| = \sqrt{(\partial H/\partial x)^2 + (\partial H/\partial y)^2}$, and the slope of the internal tide beam $s = \sqrt{\frac{\omega^2 - f^2}{N_b^2 - \omega^2}}$. N_b is the near-bottom buoyancy frequency, f is the local Coriolis frequency and ω is the tidal frequency. Thin black curves in (a)–(f) represent the same depth contours as in Figure 1, while the continuous magenta curves represent the shoreline. BCAL, SCB, SM, SCR, OR, and WSH are defined in Figure 1.

52 m. Beyond the thermocline, N^2 decreases significantly with depth over the slope. Although the N^2 profile and the location of the thermocline in the WRIT solution are similar to those of NRIT (not shown), there are some differences (Figure 13d). Overall, in the WRIT solution N^2 decreases in the first 75 m water depth followed by an increase in the next 425 m compared to the NRIT solution. Deeper than $z = -500$ m, the differences in N^2 between NRIT and WRIT solutions diminish. The differences in N^2 over the slope between the two solutions are largest nearshore (inset; Figure 13d) with a maximum increase and decrease of $+1 \times 10^{-5}$ and -2×10^{-5} s^{-2} at the surface and at 14 m depth, respectively. A maximum percent change of 9.3% in N^2 with remote IT forcing in the surface 300 m, confirms that the remote ITs do not cause drastic changes in stratification in the USWC margin as suggested in Section 3.6.

The differences in stratification between the NRIT and WRIT solutions are both due to the advection and diffusion of heat and salt. While the advection of heat and salt by the remote ITs plays the major role in the stratification changes in the surface 300 m (Figure 13h), diffusion becomes more important at larger depths (Appendix A). Because the diffusivities for the two tracers (i.e., temperature and salinity) were not stored, we make use of the vertical mixing diffusivity, κ (Equation 5) to measure if there is increase in turbulence with remote IT forcing. In the NRIT solution, areas of high vertical mixing ($\kappa \sim 10^{-2}$ $m^2 s^{-1}$) are confined to the surface and bottom boundary layers separated by a quasi-inviscid ($\kappa \sim 10^{-4}$ $m^2 s^{-1}$) interior (Figure 13e). Overall, with remote IT forcing, κ increases throughout the water column in the WRIT solution compared to the NRIT solution

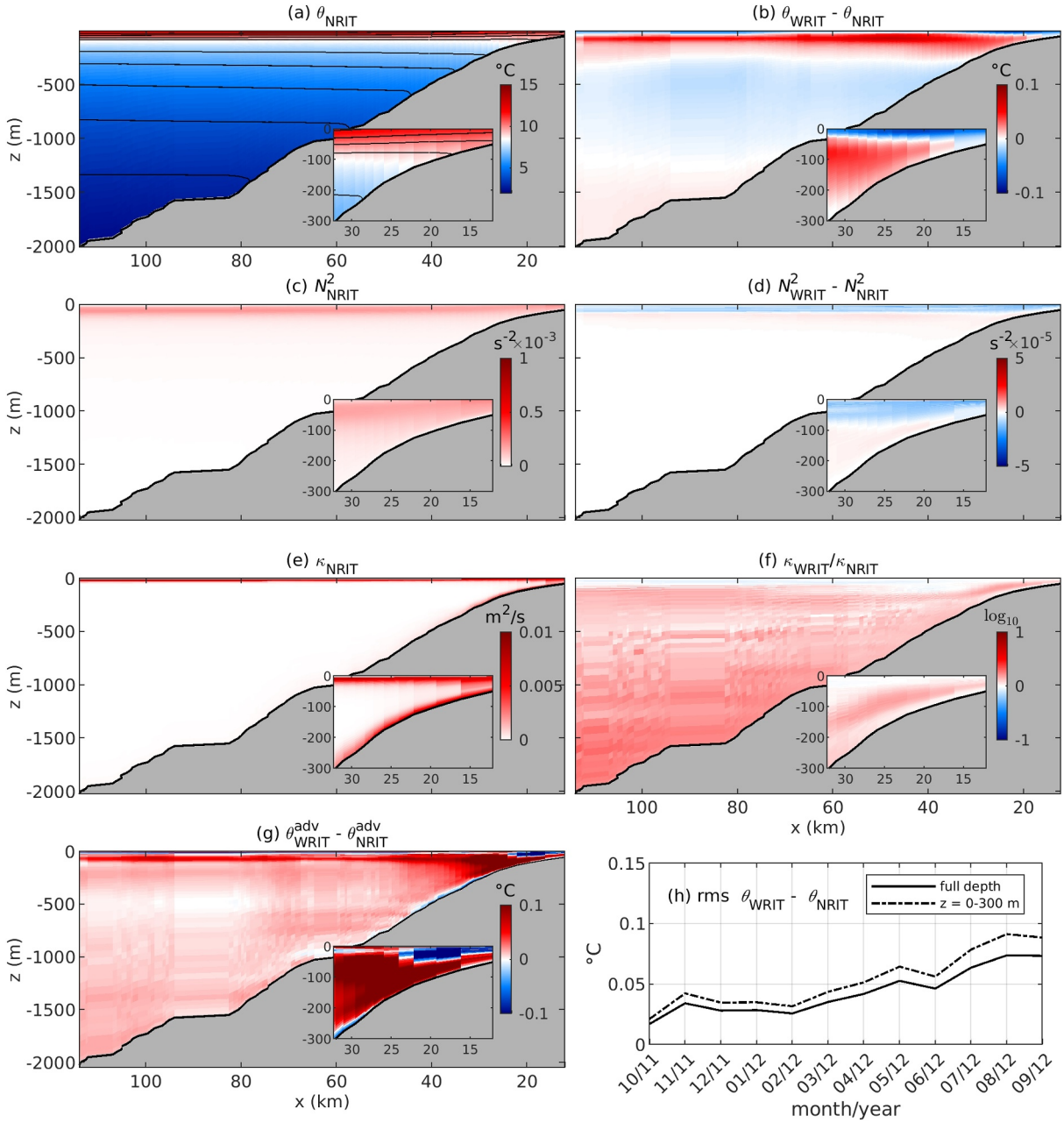

Figure 13. Time-mean (01 October 2011–30 September 2012) and along-shore averaged (a) temperature θ, (c) buoyancy frequency N^2, and (e) vertical mixing diffusivity κ (Equation 5) for the simulation without remote internal wave (IW) forcing (NRIT) for the entire USWC. The differences in (b) θ and (d) N^2 between WRIT (simulation with remote IW forcing) and NRIT. (f) The ratio between the WRIT and NRIT diffusivities ($\kappa_{WRIT}/\kappa_{NRIT}$). Panel (g) is similar to (b) but the changes are due to the contribution of temperature advection only (see Appendix A). Insets in (a)–(g) are enlarged views for $H \leq 300$ m. (h) The monthly root-mean-square (rms) temperature difference between the WRIT and NRIT solutions for the entire water column (solid, black) and the surface 300 m (dashed, black).

(Figure 13f). Nonetheless, we estimate the increase in κ to vary with depth. The increase in κ is largest at deeper depths (for $z \leq -1{,}000$ m, $\kappa_{WRIT}/\kappa_{NRIT} \approx 2$) and becomes smaller toward the surface layer. An increment of only 10% in κ in the top 300 m water depth implies that remote IT-induced diffusion plays a minor role in the stratification changes observed near the surface in Figure 13d. These changes are dominated by the advection of heat and salt (Appendix A).

Using a series of one-way nested numerical simulations, Suanda et al. (2017) also quantified the impact of shoaling baroclinic energy on temperature profiles on the Santa Maria (SM) continental shelf. Although their

shelf simulation inherited boundary conditions from a parent grid that has tidal forcing, they did not consider long range remote ITs. We estimate a remote semidiurnal IT energy flux of 256 W/m to radiate into the SM continental margin during June-July, which is ∼3 times larger than the flux from nearby rough topographies (100 W/m) in their study. We observe that the remote ITs cause cooling at the surface and warming at depth on the SM continental shelf, with a spatial rms temperature difference of ≈0.1°C. While Suanda et al. (2017) correlated increased thermal diffusivities with the temperature changes observed in their simulation, most of the changes in the SM shelf in our study are due to advection. In addition, the thermocline on the SM shelf becomes less stratified in the presence of the remote ITs. Hence, in order to achieve realistic stratification in the continental margins, future coastal regional models may also need to account for remote ITs generated across ocean basins.

5. Summary and Conclusions

In this study, we show that low-mode ITs generated at remote sources can impact the ocean dynamics along continental margins. We use a 4-km horizontal resolution regional ROMS simulation of the U.S. West Coast (USWC) with realistic tidal and atmospheric forcing. At the open boundaries, the USWC domain receives subtidal forcing from a basin scale ROMS simulation of the Northeast Pacific and high-frequency forcing including surface tides and remote IWs from a global HYCOM solution. In order to minimize IW reflections at the open boundaries, the ROMS simulation uses a 58-km wide sponge layer whose horizontal viscosity increases from 0 m^2/s at the sponge interior to 800 m^2/s at the open boundaries (Siyanbola et al., 2023). For comparison purposes, we also use a twin solution without remote IW forcing at the open boundaries.

We estimate that mode-1 semidiurnal ITs contribute an annual average of 290 W/m energy flux along the USWC continental margin. Approximately 25% of this incident energy flux comes from the Mendocino Escarpment and other nearby rough topographies, while the remaining fraction is generated by remote sources thousands of kilometers away, for example, Hawaii. We obtain these results by applying a DFT-based spatial filter to the outputs of the two regional ROMS simulations in separating the onshore and offshore propagating ITs near the USWC. Averaged over 1 year, ∼20% of the remote mode-1 semidiurnal ITs are reflected off the USWC margin back to the open ocean, ∼40% is scattered to modes 2–5, ∼7% is transmitted to the shelf and the remaining 33% is dissipated on the continental slope. Similar numbers were found by Kelly et al. (2013) but they ignored dissipation. However, these fractions vary along the USWC. While reflectivity is generally small everywhere along the USWC (<20%), reflectivity as high as 49% is observed for the Sacramento Basin. An explanation for this is that the Sacramento slope is more supercritical relative to the semidiurnal IT beams compared to the other regions along the USWC. In contrast, mode-1 IT energy scattering is significant everywhere (33%–48%) except for the Sacramento margin. The fraction of mode-1 IT energy transmitted onto the continental shelf is higher to the north of the Mendocino Escarpment (∼17%) than to the south (<10%). This is due to a stronger near-surface stratification along the Oregon-Washington coasts.

The remote ITs enhance both the advection and diffusion of temperature and salt, which causes changes in stratification in the USWC margin. Although of different magnitude along the USWC, overall we observe cooling at the surface and warming at depth with remote IW forcing. The changes in temperature in the surface 300 m are mainly due to temperature advection by the remote ITs, whereas diffusion (mixing) becomes more important for larger depths. The increase in turbulent mixing that extends several hundreds of meters above the seafloor is attributed to the increased IT energy dissipation (Martini et al., 2013; Nash et al., 2007). However, the changes in temperature and stratification at larger depths are one order of magnitude smaller compared to those in the surface 300 m. Although the USWC is not exposed to exceptionally strong remotely generated IWs that cause drastic changes in the sub-tidal stratification, we conclude that an accurate representation of stratification in the continental margins in regional simulations may require the inclusion of remotely generated IWs.

Appendix A: Remote IT-Induced Temperature Advection

In ROMS, the potential temperature tendency is a balance between temperature advection, vertical diffusion, horizontal diffusion H_{diff} and, solar and non-solar heat forcing at the ocean surface $\mathcal{F}_\theta$ (Herdström, 2009),

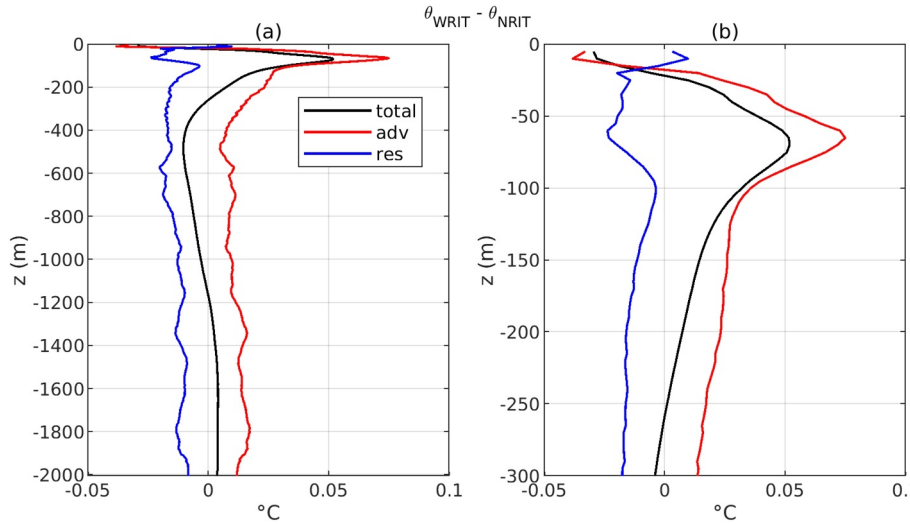

Figure A1. (a) Cross-shore averaged temperature differences between the WRIT and NRIT solutions (black curve), temperature differences due to advection only (red curve), and temperature differences due to the residual terms in Equation A1 (blue curve). Panel (b) is the enlarged view of (a) but for the surface 300 m. The residual temperature differences represent differences due to diffusion because $\mathcal{F}_\theta$ in both NRIT and WRIT solutions is similar.

$$\frac{\partial \theta}{\partial t} = -\underbrace{\left(u\frac{\partial \theta}{\partial x} + v\frac{\partial \theta}{\partial y} + w\frac{\partial \theta}{\partial z}\right)}_{\text{temp. adv.}} + \underbrace{K_\theta \frac{\partial \theta}{\partial z}}_{\text{vert. diff.}} + H_{\text{diff}} + \mathcal{F}_\theta. \tag{A1}$$

(u, v, w) represents the total velocity vector field including both low- and high-frequency motions. Of all the terms in Equation A1, we are only able to estimate the advection, surface heat forcing, and temperature tendency terms. Vertical mixing in the solutions used in this study is parameterized with the KPP model (Large et al., 1994), but the thermal diffusivities (K_θ) were not stored. Also, there is no explicit horizontal diffusion in ROMS. Most of the diffusion is associated with the third-order upstream-biased advection scheme. Hence, we estimate the contribution of the horizontal and vertical diffusion as the residual of Equation A1. We note that all the terms present in Equation A1 can be computed online and outputted in history files. However, such effort is beyond the scope of this study.

In this appendix, we show that remote IT-induced temperature advection is largely responsible for the heat redistribution in the surface 300 m in the USWC margin. To provide a quantitative comparison of the relative importance of temperature advection due to the remote ITs, we spatially average the changes in Figures 13b and 13g in the cross-shore direction (Figure A1). Averaged over the year, the change in temperature at the surface due to advection is similar to that for the total (−0.03°C). However, the thermocline is slightly warmer due to IT-induced temperature advection only (+0.07°C) compared to the combined advection-diffusion contributions (+0.05°C). As shown in Figure A1a, the remote IT-induced advection causes warming throughout the water column below the thermocline. Averaged over the water column, the root-mean-square contribution of vertical advection $\left(w\frac{\partial \theta}{\partial z}\right)$ is ∼15% larger than the horizontal advection $\left(u\frac{\partial \theta}{\partial x} + v\frac{\partial \theta}{\partial y}\right)$. However, the vertical and horizontal diffusion of temperature is responsible for the cooling observed in the 300–1,200 m depth range.

Data Availability Statement

The DFT MATLAB code "space_filt.m" used in the directional decomposition of the IT energy flux fields can be accessed on GitHub https://github.com/Oladeji17/matlab/tree/main/DFT/2D/ (Siyanbola, 2022). Samples of the model output for the ROMS simulations used in this study can be accessed online at https://doi.org/10.5281/zenodo.7194957 (Siyanbola et al., 2022).

Acknowledgments
O.Q. Siyanbola and M.C. Buijsman are supported by the National Science Foundation (NSF), USA Grant OCE1851397. M.C. Buijsman is also supported by National Aeronautic Space Administration (NASA) Grants 80NSSC18K0771 and 80NSSC20K1135, and Office of Naval Research (ONR) Grant N00014-22-1-2576. A. Delpech and R. Barkan receive funding from NSF, USA Grant OCE1851376. R. Barkan is also funded by the Israeli Science Foundation Grant 1736/18. Y. Pan acknowledges support from NSF USA Grant OCE2241495. B.K. Arbic is supported by NSF USA Grant OCE1851164. We thank the anonymous reviewers for their constructive comments which were helpful improving the manuscript.

References

Alford, M. H., MacKinnon, J. A., Simmons, H. L., & Nash, J. D. (2016). Near-inertial internal gravity waves in the ocean. *Annual Reviews*, *8*(1), 95–123. https://doi.org/10.1146/annurev-marine-010814-015746

Alford, M. H., & Zhao, Z. (2007). Global patterns of low-mode internal-wave propagation. Part I: Energy and energy flux. *Journal of Physical Oceanography*, *37*(7), 1829–1848. https://doi.org/10.1175/jpo3085.1

Arbic, B. K., Alford, M. H., Ansong, J. K., Buijsman, M. C., Ciotti, R. B., Farrar, J. T., et al. (2018). A primer on global internal tide and internal gravity wave continuum modeling in HYCOM and MITgcm. In E. Chassignet, A. Pascual, J. Tintoré, & J. Verron (Eds.), *New Frontiers in Operational Oceanography* (pp. 307–392). GOADAE OceanView.

Arbic, B. K., Garner, S. T., Hallberg, R. W., & Simmons, H. L. (2004). The accuracy of surface elevations in forward global barotropic and baroclinic tide models. *Deep-Sea Research II*, *51*(25–26), 3069–3101. https://doi.org/10.1016/j.dsr2.2004.09.014

Arbic, B. K., Richman, J. G., Shriver, J. F., Timko, P. G., Metzger, E. J., & Wallcraft, A. J. (2012). Global modeling of internal tides: Within an eddying ocean general circulation model. *Oceanography*, *25*(2), 20–29. https://doi.org/10.5670/oceanog.2012.38

Arbic, B. K., Wallcraft, A. J., & Metzger, E. J. (2010). Concurrent simulation of the eddying general circulation and tides in a global ocean model. *Ocean Modelling*, *32*(3–4), 175–187. https://doi.org/10.1016/j.ocemod.2010.01.007

Assene, F., Koch-Larrouy, A., Dadou, I., Tchilibou, M., Morvan, G., Chanut, J., et al. (2024). Internal tides off the Amazon shelf - Part I: The importance of the structuring of ocean temperature during two contrasted seasons. *EGUsphere*, *20*(1), 43–67. https://doi.org/10.5194/os-20-43-2024

Babu, C. P., Brumsack, H.-J., Schnetger, B., & Böthcher, M. E. (2002). Barium as a productivity proxy in continental margin sediments: A study from the eastern Arabian Sea. *Marine Geology*, *184*(3–4), 189–206. https://doi.org/10.1016/s0025-3227(01)00286-9

Balmforth, N. J., & Peacock, T. (2009). Tidal conversion by supercritical topography. *Journal of Physical Oceanography*, *39*(8), 1965–1974. https://doi.org/10.1175/2009jpo4057.1

Barkan, R., McWilliams, J. C., Molemaker, M. J., Choi, J., Srinivasan, K., Shchepetkin, A. F., & Bracco, A. (2017). Submesoscale dynamics in the northern Gulf of Mexico. Part II: Temperature–salinity relations and cross-shelf transport processes. *Journal of Physical Oceanography*, *47*(9), 2347–2360. https://doi.org/10.1175/jpo-d-17-0040.1

Bianchi, T. S., DiMarco, S. F., Cowan, J. H., Jr., Hetland, R. D., Chapman, P., Day, J. W., & Allison, M. A. (2010). The science of hypoxia in the northern Gulf of Mexico: A review. *Science of the Total Environment*, *408*(7), 1471–1484. https://doi.org/10.1016/j.scitotenv.2009.11.047

Bishakhdatta, G., & Sutanu, S. (2011). Direct and large-eddy simulations of internal tide generation at a near-critical slope. *Journal of Fluid Mechanics*, *681*, 48–79. https://doi.org/10.1017/jfm.2011.170

Bleck, R., Halliwell, G., Wallcraft, A., Carroll, S., Kelly, K., & Rushing, K. (2002). Hybrid coordinate ocean model (HYCOM). User's Manual (p. 211).

Buijsman, M. C., Ansong, J. K., Arbic, B. K., Richman, J. G., Shriver, J. F., Timko, P. G., et al. (2016). Impact of parameterized internal wave drag on the semidiurnal energy balance in a global ocean circulation model. *Journal of Physical Oceanography*, *46*(5), 1399–1419. https://doi.org/10.1175/jpo-d-15-0074.1

Buijsman, M. C., Arbic, B. K., Richman, J. G., Shriver, J. F., Wallcraft, A. J., & Zamudio, L. (2017). Semidiurnal internal tide incoherence in the equatorial Pacific. *Journal of Geophysical Research: Oceans*, *122*(7), 5286–5305. https://doi.org/10.1002/2016jc012590

Buijsman, M. C., Legg, S., & Klymak, J. (2012). Double-ridge internal tide interference and its effect on dissipation in Luzon Strait. *Journal of Physical Oceanography*, *42*(8), 1337–1356. https://doi.org/10.1175/jpo-d-11-0210.1

Buijsman, M. C., Stephenson, G. R., Ansong, J. K., Arbic, B. K., Green, J. A. M., Richman, J. G., et al. (2020). On the interplay between horizontal resolution and wave drag and their effect on tidal baroclinic mode waves in realistic global ocean simulations. *Ocean Modelling*, *152*, 17. https://doi.org/10.1016/j.ocemod.2020.101656

Cacchione, D. A., Pratson, L. F., & Ogston, A. S. (2002). The shaping of continental slopes by internal tides. *Science*, *296*(5568), 724–727. https://doi.org/10.1126/science.1069803

Carter, G. S., Merrifield, M. A., Becker, J. M., Katsumata, K., Gregg, M. C., Luther, D. S., et al. (2008). Energetics of M_2 barotropic to baroclinic tidal conversion at the Hawaiian Islands. *Journal of Physical Oceanography*, *38*(10), 2205–2223. https://doi.org/10.1175/2008jpo3860.1

Checkley, D. M., Jr., & Barth, J. A. (2009). Patterns and processes in the California Current System. *Progress in Oceanography*, *83*(1–4), 49–64. https://doi.org/10.1016/j.pocean.2009.07.028

Chen, H., Zhang, W., Xie, X., & Ren, J. (2019). Sediment dynamics driven by contour currents and mesoscale eddies along continental slope: A case study of the northern South China Sea. *Marine Geology*, *409*, 48–66. https://doi.org/10.1016/j.margeo.2018.12.012

Clément, L., Frajka-Williams, E., Sheen, K. L., Brearley, J. A., & Garabato, A. C. (2016). Generation of internal waves by eddies impinging on the western boundary of the North Atlantic. *Journal of Physical Oceanography*, *46*(4), 1067–1079. https://doi.org/10.1175/jpo-d-14-0241.1

Cohen, S., Kettner, A. J., & Syvitski, J. P. M. (2014). Global suspended sediment and water discharge dynamics between 1960 and 2010: Continental trends and intra-basin sensitivity. *Global and Planetary Change*, *115*, 44–58. https://doi.org/10.1016/j.gloplacha.2014.01.011

Cyriac, A., Phillips, H. E., Bindoff, N. L., & Feng, M. (2022). Characteristics of wind-generated near-inertial waves in the Southeast Indian Ocean. *Journal of Physical Oceanography*, *52*(4), 557–578. https://doi.org/10.1175/jpo-d-21-0046.1

Dauxois, T., & Young, W. R. (1999). Near-critical reflection of internal waves. *Journal of Fluid Mechanics*, *390*, 271–295. https://doi.org/10.1017/s0022112099005108

de Lavergne, C., Falahat, S., Madec, G., Roquet, F., Nycander, J., & Vic, C. (2019). Toward global maps of internal tide energy sinks. *Ocean Modelling*, *137*, 52–75. https://doi.org/10.1016/j.ocemod.2019.03.010

Delpech, A., Barkan, R., Srinivasan, K., McWilliams, J. C., Arbic, B. K., Siyanbola, O. Q., & Buijsman, M. C. (2024). Eddy-internal wave interactions and their contribution to cross-scale energy fluxes: A case study in the California Current. *Journal of Physical Oceanography*, *54*(3), 741–754. https://doi.org/10.1175/jpo-d-23-0181.1

Dorrell, R. M., Peakall, J., Summer, E. J., Parsons, D. R., Darby, S. E., Wynn, R. B., et al. (2016). Flow dynamics and mixing processes in hydraulic jump arrays: Implications for channel-lobe transition zones. *Marine Geology*, *381*, 181–193. https://doi.org/10.1016/j.margeo.2016.09.009

Dushaw, B. D., Howe, B. M., Cornuelle, B. D., Worcester, P. F., & Luther, D. S. (1995). Barotropic and baroclinic tides in the Central North Pacific Ocean determined from long-range reciprocal acoustic transmissions. *Journal of Physical Oceanography*, *25*(4), 631–647. https://doi.org/10.1175/1520-0485(1995)025<0631:babtit>2.0.co;2

Eden, C., & Olbers, D. (2014). An energy compartment model for propagation, nonlinear interaction, and dissipation of internal gravity waves. *Journal of Physical Oceanography*, *44*(8), 2093–2106. https://doi.org/10.1175/jpo-d-13-0224.1

Falahat, S., Nycander, J., Roquet, F., & Zarroug, M. (2014). Global calculation of tidal energy conversion into vertical normal modes. *Journal of Physical Oceanography*, *44*(12), 3225–3244. https://doi.org/10.1175/jpo-d-14-0002.1

Friedrichs, C. T., & Wrights, L. D. (1995). Resonant internal waves and their roles in transport and accumulation of fine sediment in Eckernförd Bay, Baltic Sea. *Continental Shelf Research*, *15*(13), 1697–1721. https://doi.org/10.1016/0278-4343(95)00035-y

Gan, J., & Allen, J. S. (2005). Modeling upwelling circulation off the Oregon coast. *Journal of Geophysical Research*, *110*(C10), C10S07. https://doi.org/10.1029/2004jc002692

Gerkema, T. (2001). Internal and interfacial tides: Beam scattering and local generation of solitary waves. *Journal of Marine Research*, *59*(2), 227–255. https://doi.org/10.1357/002224001762882646

Gerkema, T., Lam, F.-P. A., & Maas, L. R. M. (2004). Internal tides in the Bay of Biscay: Coversion rates and seasonal effects. *Deep Sea Research Part II: Topical Studeis in Oceanography*, *51*(25–26), 2995–3008. https://doi.org/10.1016/j.dsr2.2004.09.012

Gerkema, T., & Zimmerman, J. T. F. (2008). *An introduction to internal waves*. Lecture Notes. Royal Netherlands Institute for Sea Research.

Gill, A. E., & Clarke, A. J. (1974). Wind-induced upwelling, coastal currents and sea-level changes. *Deep-Sea Research*, *21*(5), 325–345. https://doi.org/10.1016/0011-7471(74)90038-2

Gong, Y., Rayson, M. D., Jones, N. L., & Ivey, G. N. (2021). Directional decomposition of internal tides propagating from multiple generation sites. *Ocean Modelling*, *162*, 18. https://doi.org/10.1016/j.ocemod.2021.101801

Gong, Y., Xie, J., Xu, J., Chen, Z., He, Y., & Cai, S. (2022). A directional decomposition method to estimate the reflection and transmission of nonlinear internal waves over a slope. *Journal of Geophysical Research: Oceans*, *127*(10), e2022JC018598. https://doi.org/10.1029/2022jc018598

Griffies, S. M., & Treguier, A. M. (2013). Ocean circulation models and modeling. In G. Siedler, S. M. Griffies, J. Gould, & J. A. Church (Eds.), *Ocean circulation and climate - A 21st century perspective* (pp. 521–551). Elsevier.

Haidvogel, D. B., Arango, H. G., K, H., Beckmann, A., Malanotte-Rizzoli, P., & Shchepetkin, A. F. (2000). Model evaluation experiments in the North Atlantic basin: Simulations in nonlinear terrain-following coordinates. *Dynamics of Atmospheres and Oceans*, *32*(3–4), 239–281. https://doi.org/10.1016/s0377-0265(00)00049-x

Hall, R. A., Huthnance, J. M., & Williams, R. G. (2013). Internal wave reflection on shelf slopes with depth-varying stratification. *Journal of Physical Oceanography*, *43*(2), 248–258. https://doi.org/10.1175/jpo-d-11-0192.1

Han, B. (2022). The energy conversion rates from eddies and mean flow into internal lee waves in the global ocean. *Journal of Oceanography and Limnology*, *40*(4), 1304–1313. https://doi.org/10.1007/s00343-021-1085-y

Herdström, K. S. (2009). Technical manual for a coupled sea-ice/ocean circulation model. *Computer Software Manual*.

Hermann, A. J., Stabeno, P. J., Haidvogel, D. B., & Musgrave, D. L. (2002). A regional tidal/subtidal circulation model of the southeastern Bering Sea: Development, sensitivity analyses and hindcasting. *Deep Sea Research Part II: Topical Studies in Oceanography*, *49*(26), 5945–5967. https://doi.org/10.1016/s0967-0645(02)00328-4

Hickey, B., Geier, S., Kachel, N., & MacFadyen, A. (2005). A bi-directional river plume: The Columbia in summer. *Continental Shelf Research*, *25*(14), 1631–1656. https://doi.org/10.1016/j.csr.2005.04.010

Hill, P. S., Fox, J. M., Crockett, J. S., Curran, K. J., Friedrichs, C. T., R, G. W., et al. (2007). Sediment delivery to the seabed on continental margins. In C. A. Nittrouer, J. A. Austin, M. E. Field, J. H. Kravitz, J. P. M. Syvitski, & P. L. Wiberg (Eds.), *Continental margin sedimentation*. John Wiley & Sons, Ltd.

Holland, D. M., Rosales, R. R., Stefanica, D., & Tabak, E. G. (2002). Internal hydraulic jumps and mixing in two-layer flows. *Journal of Fluid Mechanics*, *470*, 63–83. https://doi.org/10.1017/s002211200200188x

Jachec, S. M., Fringer, O. B., Street, R. L., & Gerritsen, M. G. (2007). Effects of grid resolution on the simulation of internal tides. *International Journal of Offshore and Polar Engineering*, *17*(02), 105–111.

Jensen, T. G., Magalhaes, J., Wijesekera, H. W., Buijsman, M., Helber, R., & Richman, J. (2020). Numerical modelling of tidally generated internal wave radiation from the Andaman Sea into the Bay of Bengal. *Deep-Sea Research Part II: Tropical Studies in Oceanography*, *172*, 104710. https://doi.org/10.1016/j.dsr2.2019.104710

Johannessen, O. M., Sandven, S., Chunchuzov, I. P., & Shuchman, R. A. (2019). Observations of internal waves generated by an anticyclonic eddy: A case study in the ice edge region of the Greenland Sea. *Tellus A: Dynamic Meteorology and Oceanography*, *71*(1), 1652881. https://doi.org/10.1080/16000870.2019.1652881

Kang, D., & Fringer, O. (2012). Energetics of barotropic and baroclinic tides in the Monterey Bay Area. *Journal of Physical Oceanography*, *42*(2), 272–290. https://doi.org/10.1175/jpo-d-11-039.1

Kelly, S. M. (2016). The vertical mode decomposition of surface and internal tides in the presence of a free surface and arbitrary topography. *Journal of Physical Oceanography*, *46*(12), 3777–3788. https://doi.org/10.1175/jpo-d-16-0131.1

Kelly, S. M., Jones, N. L., Nash, J. D., & Waterhouse, A. F. (2013). The geography of semidiurnal mode-1 internal-tide energy loss. *Geophysical Research Letters*, *40*(17), 4689–4693. https://doi.org/10.1002/grl.50872

Kelly, S. M., & Lermusiaux, P. F. J. (2016). Internal-tide interactions with the Gulf Stream and Middle Atlantic Bight shelfbreak front. *Journal of Geophysical Research: Oceans*, *121*(8), 6271–6294. https://doi.org/10.1002/2016jc011639

Kelly, S. M., Nash, J. D., Martini, K. I., Alford, M. H., & Kunze, E. (2012). The cascade of tidal energy from low to high modes on a continental slope. *Journal of Physical Oceanography*, *42*(7), 1217–1232. https://doi.org/10.1175/jpo-d-11-0231.1

Kerry, C. G., Powell, B. S., & Carter, G. S. (2013). Effects of remote generation sites on model estimates of M_2 internal tides in the Philippine Sea. *Journal of Physical Oceanography*, *43*(1), 187–204. https://doi.org/10.1175/jpo-d-12-081.1

Klymak, J. M., Pinkel, R., & Rainville, L. (2008). Direct breaking of the internal tide near topography: Keana Ridge, Hawaii. *Journal of Physical Oceanography*, *38*(2), 380–399. https://doi.org/10.1175/2007jpo3728.1

Klymak, J. M., Simmons, H. L., Braznikov, D., Kelly, S., MacKinnon, J. A., Alford, M. H., et al. (2016). Reflection of linear internal tides from realistic topography: The Tasman continental slope. *Journal of Physical Oceanography*, *46*(11), 3321–3337. https://doi.org/10.1175/jpo-d-16-0061.1

Kumar, N., Suanda, S. H., Colosi, J. A., Haas, K., Di Lorenzo, E., Miller, A. J., & Edwards, C. A. (2019). Coastal semidiurnal internal tidal incoherence in the Santa Maria basin, California: Observations and model simulations. *Journal of Geophysical Research: Oceans*, *124*(7), 5158–5179. https://doi.org/10.1029/2018jc014891

Large, W. G., McWilliams, J. C., & Downey, S. C. (1994). Oceanic vertical mixing: A review and a model with a nonlocal boundary layer parameterization. *Review of Geophysics*, *32*(4), 363–403. https://doi.org/10.1029/94rg01872

Legg, S. (2014). Scattering of low-mode internal waves at finite isolated topography. *Journal of Physical Oceanography*, *44*(1), 359–383. https://doi.org/10.1175/jpo-d-12-0241.1

Legg, S., & Adcroft, A. (2003). Internal wave breaking at concave and convex continental slopes. *Journal of Physical Oceanography*, *33*(11), 2224–2246. https://doi.org/10.1175/1520-0485(2003)033<2224:iwbaca>2.0.co;2

Lehrter, J. C., Ko, D. S., Murrell, M. C., Hagy, J. D., Schaeffer, B. A., Greene, R. M., et al. (2013). Nutrient distributions, transports, and budgets on the inner margin of a river-dominated continental shelf. *Journal of Geophysical Research: Oceans*, *118*(10), 4822–4838. https://doi.org/10.1002/jgrc.20362

Liang, C., Shang, X., & Chen, G. (2019). The vertical heat transport of internal solitory waves over the continental slope in the northern South China Sea. *Acta Oceanologica Sinica*, *38*(3), 36–44. https://doi.org/10.1007/s13131-019-1397-3

Martini, K. I., Alford, M. H., Kunze, E., Kelly, S. M., & Nash, J. D. (2011). Observations of internal tides on the Oregon continental slope. *Journal of Physical Oceanography*, *41*(9), 1772–1794. https://doi.org/10.1175/2011jpo4581.1

Martini, K. I., Alford, M. H., Kunze, E., Kelly, S. M., & Nash, J. D. (2013). Internal bores and breaking internal tides on the Oregon continental slope. *Journal of Physical Oceanography*, *43*(1), 120–139. https://doi.org/10.1175/jpo-d-12-030.1

Masunaga, E., Alford, M. H., Lucas, A. J., & Freudmann, A. R. (2023). Numerical simulations of internal tide dynamics in a steep submarine canyon. *Journal of Physical Oceanography*, *53*(11), 2669–2686. https://doi.org/10.1175/jpo-d-23-0040.1

Masunaga, E., Uchiyama, Y., Suzue, Y., & Yamazaki, H. (2018). Dynamics of internal tides over a shallow ridge investigated with a high-resolution downscaling regional ocean model. *Geophysical Research Letters*, *45*(8), 3550–3558. https://doi.org/10.1002/2017gl076916

Mazzini, P. L. F., Risien, C. M., Barth, J. A., Pierce, S. D., Erofeev, A., Dever, E. P., et al. (2015). Anomalous near-surface low-salinity pulses off the Central Oregon Coast. *Scientific Reports*, *5*(1), 17145. https://doi.org/10.1038/srep17145

Mercier, M. J., Garnier, N. B., & Dauxois, T. (2008). Reflection and diffraction of internal waves analyzed with the Hilbert transform. *Physics of Fluids*, *20*(8), 086601. https://doi.org/10.1063/1.2963136

Miramontes, E., Jouet, E., Thereau, E., Bruno, M., Penven, P., Guren, C., et al. (2020). The impact of internal wave on upper continental slopes: Insights of the Mozambican margin (southwest Indian Ocean). *Earth Surface Processes and Landforms*, *45*(6), 1469–1482. https://doi.org/10.1002/esp.4818

Moum, J. N., Caldwell, D. R., Nash, J. D., & Gunderson, G. D. (2002). Observations of boundary mixing over the continental slope. *Journal of Physical Oceanography*, *32*(7), 2113–2130. https://doi.org/10.1175/1520-0485(2002)032<2113:oobmot>2.0.co;2

Mouyen, M., Longuevergne, L., Steer, P., Crave, A., Lemoine, J.-M., Save, H., & Robin, C. (2018). Assessing modern river sediment discharge to the ocean using satellite gravimetry. *Nature Communications*, *9*, 3384. https://doi.org/10.1038/s41467-018-05921-y

Muller-Karger, F. E., Varela, R., Thunell, R., Luersson, R., Hu, C., & Walsh, J. J. (2005). The importance of continental margins in the global carbon cycle. *Geophysical Research Letters*, *32*(1), L01602. https://doi.org/10.1029/2004gl021346

Nash, J. D., Alford, M. H., Kunze, E., Martini, K., & Kelly, S. (2007). Hotspots of deep ocean mixing on the Oregon continental slope. *Geophysical Research Letters*, *34*(1), L01605. https://doi.org/10.1029/2006gl028170

Niwa, Y., & Hibiya, T. (2014). Generation of baroclinic tide energy in a global three-dimensional numerical model with different spatial grid resolutions. *Ocean Modelling*, *80*, 59–73. https://doi.org/10.1016/j.ocemod.2014.05.003

Osborn, T. R. (1980). Estimates of the local rate of vertical diffusion from dissipation measurements. *Journal of Physical Oceanography*, *10*(1), 83–89. https://doi.org/10.1175/1520-0485(1980)010<0083:eotlro>2.0.co;2

Osborne, J. J., Kurapov, A. L., Egbert, G. D., & Kosro, P. M. (2011). Spatial and temporal variability of the M_2 internal tide generation and propagation on the Oregon Shelf. *Journal of Physical Oceanography*, *41*(11), 2037–2062. https://doi.org/10.1175/jpo-d-11-02.1

Pan, Y., Haley, P. J., & Lermusiaux, P. F. J. (2021). Interactions of internal tides with a heterogeneous and rotational ocean. *Journal of Fluid Mechanics*, *920*, A18. https://doi.org/10.1017/jfm.2021.423

Petrucino, E. T., Paduan, J. D., & Rosenfeld, L. K. (2002). Numerical simulations of the internal tide in a submarine canyon. *Ocean Modelling*, *4*(3–4), 221–248. https://doi.org/10.1016/s1463-5003(02)00002-1

Rainville, L., & Pinkel, R. (2006). Propagation of low-mode internal waves through the ocean. *Journal of Physical Oceanography*, *36*(6), 1220–1236. https://doi.org/10.1175/jpo2889.1

Raja, K. J., Buijsman, M. C., Shriver, J. F., Arbic, B. K., & Siyanbola, O. Q. (2022). Near-inertial wave energetics modulated by background flows in a global model simulation. *Journal of Physical Oceanography*, *52*(5), 823–840. https://doi.org/10.1175/jpo-d-21-0130.1

Ray, R. D., & Mitchum, G. T. (1996). Surface manifestation of internal tides generated near Hawaii. *Geophysical Research Letters*, *23*(16), 2101–2104. https://doi.org/10.1029/96gl02050

Renault, L., C, M. J., Kessouri, F., Jousse, A., Frenzel, H., Chen, R., & C, D. (2021). Evaluation of high-resolution atmospheric and oceanic simulations of the California Current System. *Progress in Oceanography*, *195*, 102564.

Schindelegger, M., Kotzian, D. P., Ray, R. D., Green, J. A. M., & Stolzenberger, S. (2022). Interannual changes in tidal conversion modulate M_2 amplitudes in the Gulf of Maine. *Geophysical Research Letters*, *49*(24), e2022GL101671. https://doi.org/10.1029/2022gl101671

Shchepetkin, A. F., & McWilliams, J. C. (2003). A method for computing horizontal pressure-gradient force in an oceanic model with a nonaligned vertical coordinate. *Journal of Geophysical Research*, *108*(C3), 3090. https://doi.org/10.1029/2001jc001047

Shchepetkin, A. F., & McWilliams, J. C. (2005). The regional oceanic modeling system (ROMS): A split-explicit, free-surface, topography-following-coordinate oceanic model. *Ocean Modelling*, *9*(4), 347–404. https://doi.org/10.1016/j.ocemod.2004.08.002

Shchepetkin, A. F., & McWilliams, J. C. (2009). Correction and commentary for "Ocean Forecasting in Terrain-Following Coordinates: Formulation and Skill Assessment of the Regional Ocean Modeling System" by Haidvogel et al., J. Comp. Phys. 227, pp. 3595–3624. *Journal of Computational Physics*, *228*(24), 8985–9000. https://doi.org/10.1016/j.jcp.2009.09.002

Shen, J., Fang, W., Zhang, S., Qiu, Y., Zhang, J., & Xie, X. (2020). Observed internal tides and near-inertial waves in the Northern South China Sea: Intensified f-band energy induced by parametric subharmonic instability. *Journal of Geophysical Research: Oceans*, *125*(10), e2020JC016324. https://doi.org/10.1029/2020jc016324

Simmons, H. L., & Alford, M. H. (2012). Simulating the long-range swell of internal waves generated by ocean storms. *Oceanography*, *25*(2), 30–41. https://doi.org/10.5670/oceanog.2012.39

Siyanbola, O. Q. (2022). space_filt [Software]. *GitHub*. Retrieved from https://github.com/Oladeji17/matlab/tree/main/DFT/2D/

Siyanbola, O. Q., Buijsman, M. C., Delpech, A., Renault, L., Barkan, R., Shriver, J. F., et al. (2022). Remote internal wave forcing of regional ocean simulations near the U.S. West Coast [Dataset]. *Zenodo*. https://doi.org/10.5281/zenodo.7194957

Siyanbola, O. Q., Buijsman, M. C., Delpech, A., Renault, L., Barkan, R., Shriver, J. F., et al. (2023). Remote internal wave forcing of regional ocean simulations near the U.S. West Coast. *Ocean Modelling*, *181*, 102154. https://doi.org/10.1016/j.ocemod.2022.102154

Spicer, P., Cole, K. L., Huguenard, K., MacDonald, D. G., & Whitney, M. M. (2021). The effect of bottom-generated tidal mixing on tidally pulsed river plumes. *Journal of Physical Oceanography*, *51*, 2223–2241. https://doi.org/10.1175/jpo-d-20-0228.1

Stewart, K. D., Hogg, A. M., Griffies, S. M., Heerdegen, A. P., Ward, M. L., Spence, P., & England, M. H. (2017). Vertical resolution of baroclinic modes in global ocean models. *Ocean Modelling*, *113*, 50–65. https://doi.org/10.1016/j.ocemod.2017.03.012

Suanda, S. H., Fedderson, F., & Kumar, N. (2017). The effect of barotropic and baroclinic tides on coastal stratification and mixing. *Journal of Geophysical Research: Oceans*, *122*(12), 10156–10173. https://doi.org/10.1002/2017jc013379

Symonds, P. P., Eldholm, O., Jean, M., & Moore, G. F. (2000). Characteristics of continental margins. In P. J. Cook & C. Carleton (Eds.), *Continental shelf limits: The scientific and legal interface*. Oxford University Press.

Tchilibou, M., Koch-Larrouy, A., Barbot, S., Lyard, F., Morel, Y., Jouanno, J., & Morrow, R. (2022). Internal tides off the Amazon shelf during two contrasted seasons: Interactions with background circulation and SSH imprints. *Ocean Science*, *18*(6), 1591–1618. https://doi.org/10.5194/os-18-1591-2022

Townsend, D. W., Thomas, A. C., Mayer, L. M., Thomas, M. A., & Quinlan, J. A. (2004). Oceanography of the Northeast Atlantic continental shelf. In A. R. Robinson & K. H. Brink (Eds.), *The sea: The global ocean: Interdisciplinary regional studies and syntheses*. Harvard University Press.

Villamaña, M., Mouriño-Carbellido, B., Marañón, E., Cermeño, P., Chouciño, P., da Silva, J. C. B., et al. (2017). Role of internal waves on mixing, nutrient supply and phytoplankton community structure during spring and neap tides in the upwelling ecosystem of Ria de Vigo (NW Iberian Peninsula). *Limnology and Oceanography*, *15*, 1014–1030.

Voisin, B. (1992). Internal wave generation by turbulent wakes. In *Meeting-Workshop on Mixing in Geophysical Flows, Effects of Body Forces in Turbulent Flows* (pp. 291–301).

Wakata, Y. (2018). LES study of vertical eddy diffusivity estimation in bottom boundary layers. *Journal of Physical Oceanography*, *48*(8), 1903–1920. https://doi.org/10.1175/jpo-d-17-0165.1

Wang, S., Cao, A., Li, Q., & Chen, X. (2021). Reflection of K_1 internal tides at the continental slope in the Northern South China Sea. *Journal of Geophysical Research: Oceans*, *126*(7), e2021JC017260. https://doi.org/10.1029/2021jc017260

Wang, S., Chen, X., Li, Q., Wang, J., Meng, J., & Zhao, M. (2018). Scattering of low-mode internal tides at different shaped continental shelves. *Continental Shelf Research*, *169*, 17–24. https://doi.org/10.1016/j.csr.2018.09.010

Wang, T., Barkan, R., McWilliams, J. C., & Molemaker, M. J. (2021). Structure of submesoscale fronts of the Mississippi River plume. *Journal of Physical Oceanography*, *51*(4), 1113–1131. https://doi.org/10.1175/jpo-d-20-0191.1

Waterhouse, A. F., MacKinnon, J. A., Nash, J. D., Alford, M. H., Kunze, E., Simmons, H. L., et al. (2014). Global patterns of diapycnal mixing from measurements of the turbulent dissipation rate. *Journal of Physical Oceanography*, *37*(7), 1854–1872. https://doi.org/10.1175/jpo-d-13-0104.1

Whitney, F. A., Crawford, W. R., & Harrison, P. J. (2005). Primary processes that enhance nutrient transport and primary productivity in the coastal and open ocean of the subarctic NE Pacific. *Deep-Sea Research II*, *52*(5–6), 681–706. https://doi.org/10.1016/j.dsr2.2004.12.023

Yang, Q., Nikurashin, M., Sasaki, H., Sun, H., & Tian, J. (2019). Dissipation of mesoscale eddies and its contribution to mixing in the northern South China Sea. *Scientific Reports*, *9*(1), 556. https://doi.org/10.1038/s41598-018-36610-x

Zaron, E. D. (2019). Baroclinic tidal sea level from exact-repeat mission altimetry. *Journal of Physical Oceanography*, *49*(1), 193–210. https://doi.org/10.1175/jpo-d-18-0127.1

Zaron, E. D., & Egbert, G. D. (2014). Time-variable refraction of the internal tide at the Hawaiian Ridge. *Journal of Physical Oceanography*, *44*(2), 538–557. https://doi.org/10.1175/jpo-d-12-0238.1

Zaron, E. D., Musgrave, R. C., & Egbert, G. D. (2022). Baroclinic tidal energetics inferred from satellite altimetry. *Journal of Physical Oceanography*, *52*(5), 1015–1032. https://doi.org/10.1175/jpo-d-21-0096.1

Zhang, L., Buijsman, M. C., Comino, E., & Swinney, H. L. (2017). Internal wave generation by tidal flow over periodically and randomly distributed seamounts. *Journal of Geophysical Research: Oceans*, *15*(6), 5063–5074. https://doi.org/10.1002/2017jc012884

Zhang, L., Liu, C., Sun, W., Wang, Z., Liang, X., Li, X., & Cheng, C. (2022). Modeling mesoscale eddies generated over the continental slope, East Antarctica. *Frontiers in Earth Science*, *10*, 916398. https://doi.org/10.3389/feart.2022.916398

Zhao, Z., Alford, M. H., Girton, J. B., Rainville, L., & Simmons, H. L. (2016). Global observations of open-ocean mode-1 M_2 internal tides. *Journal of Physical Oceanography*, *44*(6), 1657–1684. https://doi.org/10.1175/jpo-d-15-0105.1

Erratum

The originally published version of this article contained a typographical error in one of the grant numbers in the Acknowledgments. The sentence "M.C. Buijsman is also supported by National Aeronautic Space Administration (NASA) Grants 80NSSC18K0771 and NNX17AH55G" should be changed to "M.C. Buijsman is also supported by National Aeronautic Space Administration (NASA) Grants 80NSSC18K0771 and 80NSSC20K1135." The error has been corrected, and this may be considered the authoritative version of record.